Nuclear Science and Techniques (2025) 36:185
https://doi.org/10.1007/s41365-025-01750-z

Production characteristics of light nuclei, hypertritons, and Ω-hypernuclei in Pb+Pb collisions at $\sqrt{s_{\mathrm{NN}}} = 5.02$ TeV

Rui-Qin Wang[1] · Xin-Lei Hou[1] · Yan-Hao Li[1] · Jun Song[2] · Feng-Lan Shao[1]

Received: 26 December 2024 / Revised: 10 February 2025 / Accepted: 16 February 2025 / Published online: 18 July 2025

Abstract

This study aims to investigate the production of light nuclei, hypertritons, and Ω-hypernuclei in Pb+Pb collisions at $\sqrt{s_{\mathrm{NN}}} = 5.02$ TeV using a modified analytical nucleon coalescence model with hyperons. To this end, the momentum distributions of two bodies coalescing into dibaryon states and of three bodies coalescing into tribaryon states are derived. Available data on coalescence factors B_2 and B_3, transverse momentum spectra, averaged transverse momenta, yield rapidity densities, and yield ratios of the deuteron, antihelium-3, antitriton, and hypertriton measured by the ALICE collaboration are explained. Productions of different species of Ω-hypernuclei $H(\mathrm{p}\Omega^-)$, $H(\mathrm{n}\Omega^-)$, and $H(\mathrm{pn}\Omega^-)$ are predicted. Particularly, the production correlations of different light (hyper-)nuclei are studied, and two groups of interesting observables—the averaged transverse momentum ratios of light (hyper-)nuclei to protons (hyperons) and their corresponding yield ratios—are studied. The averaged transverse momentum ratio group exhibits a reverse hierarchy of the nucleus size, and the yield raito group is sensitive to the nucleus production mechanism as well as the size of the nucleus.

Keywords Light nucleus production · Hypernucleus production · Coalescence model · Relativistic heavy ion collision

1 Introduction

In ultra-relativistic heavy ion collisions, light nuclei and hypernuclei such as deuteron (d), helium-3 (^{3}He), triton (t), and hypertriton ($^3_\Lambda$H) are produced as a special group of observables [1–5]. These groups comprise composite clusters, and their production mechanism is still debated [6–8]. Production mechanisms of such composite objects face many fundamental issues in relativistic heavy ion community; e.g., the hadronization mechanism [9], hadronic rescattering effect [10], structure of the quantum chromodynamics phase diagram [11–15], local baryon-strangeness correlation [16, 17], system freeze-out characteristics [18–20], hyperon–nucleon interaction [21, 22], and search for more hadronic molecular states [23, 24].

The production mechanisms of light nuclei and hypernuclei in ultra-relativistic heavy ion collisions have attracted considerable attention in experimental [25–28] and theoretical [29–32] research in the last few decades. The STAR experiment at the BNL Relativistic Heavy Ion Collider (RHIC) and the ALICE experiment at the CERN Large Hadron Collider (LHC) have been conducted to measure light nuclei [33–37] and hypernuclei [38–40]. Theoretical research has considered two popular production mechanisms: the thermal production mechanism [41–45] and the coalescence mechanism [46–50], which have been proven to be successful in describing the formation of such composite objects.

The coalescence mechanism, assuming light nuclei and hypernuclei are produced by the coalescence of the adjacent nucleons and hyperons in the phase space, exhibits certain unique characteristics such as the mass number

---

This work was supported by the National Natural Science Foundation of China (Nos. 12175115 and 12375074).

✉ Rui-Qin Wang
wangrq@qfnu.edu.cn

✉ Jun Song
songjun2011@jnxy.edu.cn

✉ Feng-Lan Shao
shaofl@mail.sdu.edu.cn

[1] School of Physics and Physical Engineering, Qufu Normal University, Qufu 273165, China

[2] School of Physical Science and Intelligent Engineering, Jining University, Qufu 273155, China

scaling property [51–53] and nontrivial coalescence factor behavior [54–57]. To understand the extent to which these characteristics depend on the particular coalescence models used in obtaining these characteristics, we have developed an analytical model for describing the productions of different species of light nuclei, as reported in our previous works [58–61]. We applied the developed analytical nucleon coalescence model to Au+Au collisions at the RHIC to successfully explain the energy-dependent behaviors of d, t, ^{3}He, and ^{4}He [58, 59]. We also applied the model to pp, p+Pb, and Pb+Pb collisions at the LHC to understand different behaviors of coalescence factors B_2 and B_3 [60] from small to large collision systems, and a series of concise production correlations of d, ^{3}He, and t [61] were presented.

Recently, the ALICE collaboration published the most precise measurements of d, ^{3}He, t, and especially $^3_\Lambda$H in Pb+Pb collisions at $\sqrt{s_{\rm NN}} = 5.02$ TeV to date [62–64]. In this study, we extend the coalescence model considering the coordinate–momentum correlation [61] to include the hyperon coalescence besides the nucleon coalescence and apply it to simultaneously study the productions of light nuclei, $^3_\Lambda$H, and Ω-hypernuclei. This study primarily aims to present a comprehensive overview of the latest data published in Pb+Pb collisions with the highest collision energy. The study also aims to explain the production characteristics, specifically, the production correlations of light nuclei and hypernuclei originating from the coalescence. We propose two groups of interesting observables–the averaged transverse momentum ratios and centrality-dependent yield ratios of light nuclei to protons and hypernuclei to hyperons. These ratios tend to offset the differences in the primordial p, Λ, and Ω^-, making them potent to reveal the existence of a universal production mechanism for different species of nuclei in light and strange sectors. These ratios are found to exhibit certain relationships, which are considerably different from those observed in the thermal production mechanism.

The remainder of this manuscript is organized as follows: Section 2 introduces the coalescence model and presents the formulae of the momentum distributions of two baryons coalescing into dibaryon states and three baryons coalescing into tribaryon states. Section 3 presents the behaviors of B_2 and B_3 evaluated as functions of the collision centrality and the transverse momentum per nucleon. Furthermore, the transverse momentum (p_T) spectra, averaged transverse momenta $\langle p_T \rangle$, yield rapidity densities dN/dy, and yield ratios of d, $^3\overline{\rm He}$, and $\bar{\rm t}$ are presented. Section 4 presents the results of the $^3_\Lambda$H and Ω-hypernuclei. Specifically, the averaged transverse momentum ratios $\frac{\langle p_T\rangle_{\rm d}}{\langle p_T\rangle_{\rm p}}$, $\frac{\langle p_T\rangle_{H({\rm p}\Omega^-)}}{\langle p_T\rangle_{\Omega^-}}$, $\frac{\langle p_T\rangle_{H({\rm n}\Omega^-)}}{\langle p_T\rangle_{\Omega^-}}$, $\frac{\langle p_T\rangle_{\rm t}}{\langle p_T\rangle_{\rm p}}$, $\frac{\langle p_T\rangle_{^3{\rm He}}}{\langle p_T\rangle_{\rm p}}$, $\frac{\langle p_T\rangle_{^3_\Lambda{\rm H}}}{\langle p_T\rangle_{\Lambda}}$, $\frac{\langle p_T\rangle_{H({\rm pn}\Omega^-)}}{\langle p_T\rangle_{\Omega^-}}$, and centrality-dependent behaviors of yield ratios $\frac{\rm d}{\rm p}$, $\frac{H({\rm p}\Omega^-)}{\Omega^-}$, $\frac{H({\rm n}\Omega^-)}{\Omega^-}$, $\frac{\rm t}{\rm p}$, $\frac{^3{\rm He}}{\rm p}$, $\frac{^3_\Lambda{\rm H}}{\Lambda}$, and $\frac{H({\rm pn}\Omega^-)}{\Omega^-}$ are evaluated. Finally, Section 5 presents the conclusions drawn from the study findings.

2 Coalescence model

This section presents the extension of the analytical nucleon coalescence model developed in our previous work [61] to include the hyperon coalescence. The current model executes the coalescence process on an equivalent kinetic freeze-out surface formed from different times. To realize the analytical and intuitive insights, we eliminate the systematic time-evolution execution and utilize the finite emission duration in an effective volume. First, the formalism of two baryons coalescing into d-like dibaryon states is given. Subsequently, an analytical expression of three baryons coalescing into ^{3}He, t, and their partners in the strange sector is presented.

2.1 Formalism of two bodies coalescing into dibaryon states

Starting with a hadronic system produced at the final stage of the evolution of high-energy collisions, we consider that the dibaryon state $\rm H_j$ is formed via the coalescence of two baryons $\rm h_1$ and $\rm h_2$. We use $f_{{\rm H}_j}(\boldsymbol{p})$ to denote the three-dimensional momentum distribution of the produced $\rm H_j$, as follows:

$$f_{{\rm H}_j}(\boldsymbol{p}) = \int {\rm d}\boldsymbol{x}_1{\rm d}\boldsymbol{x}_2{\rm d}\boldsymbol{p}_1{\rm d}\boldsymbol{p}_2 f_{{\rm h}_1{\rm h}_2}(\boldsymbol{x}_1,\boldsymbol{x}_2;\boldsymbol{p}_1,\boldsymbol{p}_2) \times \mathcal{R}_{{\rm H}_j}(\boldsymbol{x}_1,\boldsymbol{x}_2;\boldsymbol{p}_1,\boldsymbol{p}_2,\boldsymbol{p}). \tag{1}$$

Here, $f_{{\rm h}_1{\rm h}_2}(\boldsymbol{x}_1,\boldsymbol{x}_2;\boldsymbol{p}_1,\boldsymbol{p}_2)$ is the two-baryon joint coordinate–momentum distribution and $\mathcal{R}_{{\rm H}_j}(\boldsymbol{x}_1,\boldsymbol{x}_2;\boldsymbol{p}_1,\boldsymbol{p}_2,\boldsymbol{p})$ is the kernel function of the $\rm H_j$. Hereinafter, we use bold symbols to denote three-dimensional coordinates and momentum vectors.

In terms of the normalized joint coordinate–momentum distribution denoted by the superscript '(n)', we have

$$f_{{\rm H}_j}(\boldsymbol{p}) = N_{{\rm h}_1{\rm h}_2} \int {\rm d}\boldsymbol{x}_1{\rm d}\boldsymbol{x}_2{\rm d}\boldsymbol{p}_1{\rm d}\boldsymbol{p}_2 f^{(n)}_{{\rm h}_1{\rm h}_2}(\boldsymbol{x}_1,\boldsymbol{x}_2;\boldsymbol{p}_1,\boldsymbol{p}_2) \times \mathcal{R}_{{\rm H}_j}(\boldsymbol{x}_1,\boldsymbol{x}_2;\boldsymbol{p}_1,\boldsymbol{p}_2,\boldsymbol{p}). \tag{2}$$

Here, $N_{\mathrm{h}_1\mathrm{h}_2} = N_{\mathrm{h}_1}N_{\mathrm{h}_2}$ is the number of all possible $\mathrm{h}_1\mathrm{h}_2$-pairs in the considered hadronic system, and N_{h_i} $(i = 1, 2)$ is the number of the baryons h_i.

The kernel function $\mathcal{R}_{\mathrm{H}_j}(\boldsymbol{x}_1,\boldsymbol{x}_2;\boldsymbol{p}_1,\boldsymbol{p}_2,\boldsymbol{p})$ denotes the probability density for h_1, h_2 with momenta $\boldsymbol{p}_1$ and $\boldsymbol{p}_2$ at $\boldsymbol{x}_1$ and $\boldsymbol{x}_2$ to combine into an H_j of momentum $\boldsymbol{p}$. It carries the kinetic and dynamical information of h_1 and h_2 combining into H_j, and its precise expression should be constrained by laws such as the momentum conservation and constraints due to intrinsic quantum numbers; e.g., spin [58–61]. To consider these constraints explicitly, we rewrite the kernel function in the following form:

$$\mathcal{R}_{\mathrm{H}_j}(\boldsymbol{x}_1,\boldsymbol{x}_2;\boldsymbol{p}_1,\boldsymbol{p}_2,\boldsymbol{p}) = g_{\mathrm{H}_j}\mathcal{R}^{(x,p)}_{\mathrm{H}_j}(\boldsymbol{x}_1,\boldsymbol{x}_2;\boldsymbol{p}_1,\boldsymbol{p}_2) \times \delta\left(\sum_{i=1}^{2}\boldsymbol{p}_i - \boldsymbol{p}\right). \tag{3}$$

The spin degeneracy factor $g_{\mathrm{H}_j} = (2J_{\mathrm{H}_j} + 1)\Big/\left[\prod_{i=1}^{2}(2J_{\mathrm{h}_i} + 1)\right]$, where J_{H_j} is the spin of the produced H_j and J_{h_i} is that of the primordial baryon h_i. The Dirac δ function guarantees momentum conservation in the coalescence process. The remaining $\mathcal{R}^{(x,p)}_{\mathrm{H}_j}(\boldsymbol{x}_1,\boldsymbol{x}_2;\boldsymbol{p}_1,\boldsymbol{p}_2)$ can be solved using the Wigner transformation as the H_j wave function is given. Considering the wave function of a spherical harmonic oscillator is particularly tractable and useful for analytical insights, therefore, we adopt this profile as reported in Refs. [65–67] and have

$$\mathcal{R}^{(x,p)}_{\mathrm{H}_j}(\boldsymbol{x}_1,\boldsymbol{x}_2;\boldsymbol{p}_1,\boldsymbol{p}_2) = 8e^{-\frac{(\boldsymbol{x}'_1-\boldsymbol{x}'_2)^2}{2\sigma^2}}e^{-\frac{2\sigma^2(m_2\boldsymbol{p}'_1-m_1\boldsymbol{p}'_2)^2}{(m_1+m_2)^2}}. \tag{4}$$

The superscript ‘$'$’ in the coordinate or momentum variables denotes the baryon coordinate or momentum in the rest frame of $\mathrm{h}_1\mathrm{h}_2$-pair. Moreover, m_1 and m_2 represent the mass of h_1 and that of h_2, respectively. The width parameter $\sigma = \sqrt{\frac{2(m_1+m_2)^2}{3(m_1^2+m_2^2)}}R_{\mathrm{H}_j}$, where R_{H_j} is the root-mean-square radius of the H_j.

Substituting Eqs. (3) and (4) into Eq. (2), we have

$$f_{\mathrm{H}_j}(\boldsymbol{p}) = N_{\mathrm{h}_1\mathrm{h}_2}g_{\mathrm{H}_j}\int \mathrm{d}\boldsymbol{x}_1\mathrm{d}\boldsymbol{x}_2\mathrm{d}\boldsymbol{p}_1\mathrm{d}\boldsymbol{p}_2 f^{(n)}_{\mathrm{h}_1\mathrm{h}_2}(\boldsymbol{x}_1,\boldsymbol{x}_2;\boldsymbol{p}_1,\boldsymbol{p}_2) \times 8e^{-\frac{(\boldsymbol{x}'_1-\boldsymbol{x}'_2)^2}{2\sigma^2}}e^{-\frac{2\sigma^2(m_2\boldsymbol{p}'_1-m_1\boldsymbol{p}'_2)^2}{(m_1+m_2)^2}}\delta\left(\sum_{i=1}^{2}\boldsymbol{p}_i - \boldsymbol{p}\right). \tag{5}$$

This is the general formalism of the H_j production via the coalescence of two baryons h_1 and h_2.

Notably, the root-mean-square radius R_{H_j} of the dibaryon state H_j is always about or larger than 2 fm, and σ is considerably larger than R_{H_j}. Thus, the Gaussian width in the momentum-dependent part of the kernel function in Eq. (5) has a small value, about or smaller than 0.1 GeV/c. Therefore, we approximate the Gaussian form of the momentum-dependent kernel function to be a δ function as follows:

$$e^{-\frac{\left(\boldsymbol{p}'_1-\frac{m_1}{m_2}\boldsymbol{p}'_2\right)^2}{\left(1+\frac{m_1}{m_2}\right)^2\Big/(2\sigma^2)}} \approx \left[\frac{\sqrt{\pi}}{\sqrt{2}\sigma}\left(1+\frac{m_1}{m_2}\right)\right]^3\delta\left(\boldsymbol{p}'_1 - \frac{m_1}{m_2}\boldsymbol{p}'_2\right). \tag{6}$$

The robustness of the δ function approximation has been checked at the outset of the analytical coalescence model in our previous work [60]. Substituting Eq. (6) into Eq. (5) and integrating $\boldsymbol{p}_1$ and $\boldsymbol{p}_2$, we obtain

$$\begin{aligned}
f_{\mathrm{H}_j}(\boldsymbol{p}) &= N_{\mathrm{h}_1\mathrm{h}_2}g_{\mathrm{H}_j}\int \mathrm{d}\boldsymbol{x}_1\mathrm{d}\boldsymbol{x}_2\mathrm{d}\boldsymbol{p}_1\mathrm{d}\boldsymbol{p}_2 \\
&\quad f^{(n)}_{\mathrm{h}_1\mathrm{h}_2}(\boldsymbol{x}_1,\boldsymbol{x}_2;\boldsymbol{p}_1,\boldsymbol{p}_2)8e^{-\frac{(\boldsymbol{x}'_1-\boldsymbol{x}'_2)^2}{2\sigma^2}}\left(\frac{\sqrt{\pi}}{\sqrt{2}\sigma}\right)^3\left(1+\frac{m_1}{m_2}\right)^3 \\
&\quad \times\delta\left(\boldsymbol{p}'_1 - \frac{m_1}{m_2}\boldsymbol{p}'_2\right)\delta\left(\sum_{i=1}^{2}\boldsymbol{p}_i - \boldsymbol{p}\right) \\
&= N_{\mathrm{h}_1\mathrm{h}_2}g_{\mathrm{H}_j}\int \mathrm{d}\boldsymbol{x}_1\mathrm{d}\boldsymbol{x}_2\mathrm{d}\boldsymbol{p}_1\mathrm{d}\boldsymbol{p}_2 f^{(n)}_{\mathrm{h}_1\mathrm{h}_2}(\boldsymbol{x}_1,\boldsymbol{x}_2;\boldsymbol{p}_1,\boldsymbol{p}_2) \\
&\quad \times 8e^{-\frac{(\boldsymbol{x}'_1-\boldsymbol{x}'_2)^2}{2\sigma^2}}\left(\frac{\sqrt{\pi}}{\sqrt{2}\sigma}\right)^3\left(1+\frac{m_1}{m_2}\right)^3\gamma\delta\left(\boldsymbol{p}_1 - \frac{m_1}{m_2}\boldsymbol{p}_2\right) \\
&\quad \times\delta\left(\sum_{i=1}^{2}\boldsymbol{p}_i - \boldsymbol{p}\right) \\
&= N_{\mathrm{h}_1\mathrm{h}_2}g_{\mathrm{H}_j}\gamma\left(\frac{\sqrt{\pi}}{\sqrt{2}\sigma}\right)^3 \times 8\int \mathrm{d}\boldsymbol{x}_1\mathrm{d}\boldsymbol{x}_2 \\
&\quad f^{(n)}_{\mathrm{h}_1\mathrm{h}_2}\left(\boldsymbol{x}_1,\boldsymbol{x}_2;\frac{m_1\boldsymbol{p}}{m_1+m_2},\frac{m_2\boldsymbol{p}}{m_1+m_2}\right)e^{-\frac{(\boldsymbol{x}'_1-\boldsymbol{x}'_2)^2}{2\sigma^2}}.
\end{aligned} \tag{7}$$

Here, γ denotes the Lorentz contraction factor corresponding to the three-dimensional velocity $\boldsymbol{\beta}$ of the center-of-mass frame of the $\mathrm{h}_1\mathrm{h}_2$-pair in the laboratory frame, and the momentum transformation parallel to $\boldsymbol{\beta}$ is $p'_{1//} - \frac{m_1}{m_2}p'_{2//} = \frac{1}{\gamma}\left(p_{1//} - \frac{m_1}{m_2}p_{2//}\right)$ and that perpendicular to $\boldsymbol{\beta}$ is invariant.

Changing coordinate variables in Eq. (7) to $\boldsymbol{X} = \frac{\sqrt{2}(m_1\boldsymbol{x}_1+m_2\boldsymbol{x}_2)}{m_1+m_2}$ and $\boldsymbol{r} = \frac{\boldsymbol{x}_1-\boldsymbol{x}_2}{\sqrt{2}}$ gives

$$f_{\mathrm{H}_j}(\boldsymbol{p}) = N_{\mathrm{h}_1\mathrm{h}_2}g_{\mathrm{H}_j}\gamma\left(\frac{\sqrt{\pi}}{\sqrt{2}\sigma}\right)^3 \times 8\int \mathrm{d}\boldsymbol{X}\mathrm{d}\boldsymbol{r}f^{(n)}_{\mathrm{h}_1\mathrm{h}_2}\left(\boldsymbol{X},\boldsymbol{r};\frac{m_1\boldsymbol{p}}{m_1+m_2},\frac{m_2\boldsymbol{p}}{m_1+m_2}\right)e^{-\frac{\boldsymbol{r}'^2}{\sigma^2}}. \tag{8}$$

Considering the strong interaction and coalescence to be local, we neglect the effect of collective motion on the center of mass coordinate and assume it is factorized as

$$f^{(n)}_{\mathrm{h_1h_2}}\left(\boldsymbol{X},\boldsymbol{r};\frac{m_1\boldsymbol{p}}{m_1+m_2},\frac{m_2\boldsymbol{p}}{m_1+m_2}\right)=f^{(n)}_{\mathrm{h_1h_2}}(\boldsymbol{X}) \times f^{(n)}_{\mathrm{h_1h_2}}\left(\boldsymbol{r};\frac{m_1\boldsymbol{p}}{m_1+m_2},\frac{m_2\boldsymbol{p}}{m_1+m_2}\right). \tag{9}$$

Substituting Eq. (9) into Eq. (8), we have

$$f_{\mathrm{H}_j}(\boldsymbol{p})=N_{\mathrm{h_1h_2}}g_{\mathrm{H}_j}\gamma\left(\frac{\sqrt{\pi}}{\sqrt{2}\sigma}\right)^3 \times 8\int \mathrm{d}\boldsymbol{r}f^{(n)}_{\mathrm{h_1h_2}}\left(\boldsymbol{r};\frac{m_1\boldsymbol{p}}{m_1+m_2},\frac{m_2\boldsymbol{p}}{m_1+m_2}\right)e^{-\frac{r'^2}{\sigma^2}}. \tag{10}$$

We adopt the frequently-used Gaussian form for the relative coordinate distribution, as reported in Refs. [68–70], as follows:

$$f^{(n)}_{\mathrm{h_1h_2}}\left(\boldsymbol{r};\frac{m_1\boldsymbol{p}}{m_1+m_2},\frac{m_2\boldsymbol{p}}{m_1+m_2}\right)=\frac{1}{\left[\pi C_0R_f^2(\boldsymbol{p})\right]^{3/2}} \times e^{-\frac{\boldsymbol{r}^2}{C_0R_f^2(\boldsymbol{p})}}f^{(n)}_{\mathrm{h_1h_2}}\left(\frac{m_1\boldsymbol{p}}{m_1+m_2},\frac{m_2\boldsymbol{p}}{m_1+m_2}\right). \tag{11}$$

Here, $R_\mathrm{f}(\boldsymbol{p})$ is the effective radius of the hadronic source system at the H_j freeze-out, and C_0 is introduced to make $\boldsymbol{r}^2/C_0$ to be the square of one-half of the relative position and is equal to 2 [68–70]. In this case, $R_\mathrm{f}(\boldsymbol{p})$ is the Hanbury–Brown–Twiss (HBT) interferometry radius, which can be extracted from the two-particle femtoscopic correlations [69, 70].

With instantaneous coalescence in the rest frame of the $\mathrm{h_1h_2}$-pair, i.e., $\Delta t'=0$, we get the coordinate transformation

$$\boldsymbol{r}=\boldsymbol{r}'+(\gamma-1)\frac{\boldsymbol{r}'\cdot\boldsymbol{\beta}}{\beta^2}\boldsymbol{\beta}. \tag{12}$$

The instantaneous coalescence is a basic assumption in coalescence-like models, wherein the overlap of the nucleus Wigner phase–space density with the constituent phase–space distributions is adopted [65]. Considering the coalescence criterion judging in the rest frame is more general than in the laboratory frame, we choose the instantaneous coalescence in the rest frame of the $\mathrm{h_1h_2}$-pair, as reported in Refs. [65, 71]. Substituting Eq. (11) into Eq. (10) and using Eq. (12) to integrate from the relative coordinate variable, we obtain

$$f_{\mathrm{H}_j}(\boldsymbol{p})=\frac{8\pi^{3/2}g_{\mathrm{H}_j}\gamma}{2^{3/2}\left[C_0R_\mathrm{f}^2(\boldsymbol{p})+\sigma^2\right]\sqrt{C_0[R_\mathrm{f}(\boldsymbol{p})/\gamma]^2+\sigma^2}} \times f_{\mathrm{h_1h_2}}\left(\frac{m_1\boldsymbol{p}}{m_1+m_2},\frac{m_2\boldsymbol{p}}{m_1+m_2}\right). \tag{13}$$

Ignoring the correlations between h_1 and h_2, we obtain the three-dimensional momentum distribution of the H_j as

$$f_{\mathrm{H}_j}(\boldsymbol{p})=\frac{8\pi^{3/2}g_{\mathrm{H}_j}\gamma}{2^{3/2}\left[C_0R_\mathrm{f}^2(\boldsymbol{p})+\sigma^2\right]\sqrt{C_0[R_\mathrm{f}(\boldsymbol{p})/\gamma]^2+\sigma^2}} \times f_{\mathrm{h}_1}\left(\frac{m_1\boldsymbol{p}}{m_1+m_2}\right)f_{\mathrm{h}_2}\left(\frac{m_2\boldsymbol{p}}{m_1+m_2}\right). \tag{14}$$

Denoting the Lorentz invariant momentum distribution $E\frac{\mathrm{d}^3N}{\mathrm{d}\boldsymbol{p}^3}=\frac{\mathrm{d}^2N}{2\pi p_\mathrm{T}\mathrm{d}p_\mathrm{T}\mathrm{d}y}$ with $f^{(\mathrm{inv})}$, we finally get

$$f^{(\mathrm{inv})}_{\mathrm{H}_j}(p_\mathrm{T},y)=\frac{8\pi^{3/2}g_{\mathrm{H}_j}}{2^{3/2}\left[C_0R_\mathrm{f}^2(p_\mathrm{T},y)+\sigma^2\right]\sqrt{C_0\frac{R_\mathrm{f}^2(p_\mathrm{T},y)}{\gamma^2}+\sigma^2}} \times\frac{m_{\mathrm{H}_j}}{m_1m_2}f^{(\mathrm{inv})}_{\mathrm{h}_1}\left(\frac{m_1p_\mathrm{T}}{m_1+m_2},y\right)f^{(\mathrm{inv})}_{\mathrm{h}_2}\left(\frac{m_2p_\mathrm{T}}{m_1+m_2},y\right), \tag{15}$$

where y is the longitudinal rapidity and m_{H_j} is the mass of H_j .

2.2 Formalism of three bodies coalescing into tribaryon states

For tribaryon state H_j formed via the coalescence of three baryons h_1, h_2, and h_3, the momentum distribution $f_{\mathrm{H}_j}(\boldsymbol{p})$ is

$$f_{\mathrm{H}_j}(\boldsymbol{p})=N_{\mathrm{h_1h_2h_3}}\int \mathrm{d}\boldsymbol{x}_1\mathrm{d}\boldsymbol{x}_2\mathrm{d}\boldsymbol{x}_3\mathrm{d}\boldsymbol{p}_1\mathrm{d}\boldsymbol{p}_2\mathrm{d}\boldsymbol{p}_3f^{(n)}_{\mathrm{h_1h_2h_3}} (\boldsymbol{x}_1,\boldsymbol{x}_2,\boldsymbol{x}_3;\boldsymbol{p}_1,\boldsymbol{p}_2,\boldsymbol{p}_3)\mathcal{R}_{\mathrm{H}_j}(\boldsymbol{x}_1,\boldsymbol{x}_2,\boldsymbol{x}_3;\boldsymbol{p}_1,\boldsymbol{p}_2,\boldsymbol{p}_3,\boldsymbol{p}). \tag{16}$$

Here, $N_{\mathrm{h_1h_2h_3}}$ is the number of all possible $\mathrm{h_1h_2h_3}$-clusters and equals to $N_{\mathrm{h}_1}N_{\mathrm{h}_2}N_{\mathrm{h}_3}$, $N_{\mathrm{h}_1}(N_{\mathrm{h}_1}-1)N_{\mathrm{h}_3}$ for $\mathrm{h}_1\neq\mathrm{h}_2\neq\mathrm{h}_3$, and $\mathrm{h}_1=\mathrm{h}_2\neq\mathrm{h}_3$. Moreover, $f^{(n)}_{\mathrm{h_1h_2h_3}}(\boldsymbol{x}_1,\boldsymbol{x}_2,\boldsymbol{x}_3;\boldsymbol{p}_1,\boldsymbol{p}_2,\boldsymbol{p}_3)$ is the normalized three-baryon joint coordinate–momentum distribution, and $\mathcal{R}_{\mathrm{H}_j}(\boldsymbol{x}_1,\boldsymbol{x}_2,\boldsymbol{x}_3;\boldsymbol{p}_1,\boldsymbol{p}_2,\boldsymbol{p}_3,\boldsymbol{p})$ is the kernel function.

The kernel function can be modified as

$$\mathcal{R}_{\mathrm{H}_j}(\boldsymbol{x}_1,\boldsymbol{x}_2,\boldsymbol{x}_3;\boldsymbol{p}_1,\boldsymbol{p}_2,\boldsymbol{p}_3,\boldsymbol{p}) = g_{\mathrm{H}_j}\mathcal{R}^{(x,p)}_{\mathrm{H}_j}(\boldsymbol{x}_1,\boldsymbol{x}_2,\boldsymbol{x}_3;\boldsymbol{p}_1,\boldsymbol{p}_2,\boldsymbol{p}_3)\delta\left(\sum_{i=1}^{3}\boldsymbol{p}_i-\boldsymbol{p}\right). \tag{17}$$

The spin degeneracy factor $g_{\mathrm{H}_j}=(2J_{\mathrm{H}_j}+1)\Big/\left[\prod_{i=1}^{3}(2J_{\mathrm{h}_i}+1)\right]$. The Dirac δ function guarantees momentum conservation. Solving from the Wigner transformation [65–67], $\mathcal{R}^{(x,p)}_{\mathrm{H}_j}(\boldsymbol{x}_1,\boldsymbol{x}_2,\boldsymbol{x}_3;\boldsymbol{p}_1,\boldsymbol{p}_2,\boldsymbol{p}_3)$ is

$$\mathcal{R}^{(x,p)}_{\mathrm{H}_j}(\boldsymbol{x}_1,\boldsymbol{x}_2,\boldsymbol{x}_3;\boldsymbol{p}_1,\boldsymbol{p}_2,\boldsymbol{p}_3) = 8^2 e^{-\frac{(\boldsymbol{x}'_1-\boldsymbol{x}'_2)^2}{2\sigma_1^2}} e^{-\frac{2(\frac{m_1\boldsymbol{x}'_1}{m_1+m_2}+\frac{m_2\boldsymbol{x}'_2}{m_1+m_2}-\boldsymbol{x}'_3)^2}{3\sigma_2^2}} e^{-\frac{2\sigma_1^2(m_2\boldsymbol{p}'_1-m_1\boldsymbol{p}'_2)^2}{(m_1+m_2)^2}} e^{-\frac{3\sigma_2^2[m_3\boldsymbol{p}'_1+m_3\boldsymbol{p}'_2-(m_1+m_2)\boldsymbol{p}'_3]^2}{2(m_1+m_2+m_3)^2}}. \tag{18}$$

Here, the superscript '$'$' denotes the baryon coordinate or momentum in the rest frame of the $\mathrm{h}_1\mathrm{h}_2\mathrm{h}_3$-cluster. The width parameter $\sigma_1=\sqrt{\frac{m_3(m_1+m_2)(m_1+m_2+m_3)}{m_1m_2(m_1+m_2)+m_2m_3(m_2+m_3)+m_3m_1(m_3+m_1)}}R_{\mathrm{H}_j}$, and $\sigma_2=\sqrt{\frac{4m_1m_2(m_1+m_2+m_3)^2}{3(m_1+m_2)[m_1m_2(m_1+m_2)+m_2m_3(m_2+m_3)+m_3m_1(m_3+m_1)]}}R_{\mathrm{H}_j}$, where R_{H_j} is the root-mean-square radius of the H_j. Substituting Eqs. (17) and (18) into Eq. (16), we obtain

$$\begin{aligned} f_{\mathrm{H}_j}(\boldsymbol{p}) &= 8^2 N_{\mathrm{h}_1\mathrm{h}_2\mathrm{h}_3} g_{\mathrm{H}_j} \int \mathrm{d}\boldsymbol{x}_1\mathrm{d}\boldsymbol{x}_2\mathrm{d}\boldsymbol{x}_3\mathrm{d}\boldsymbol{p}_1\mathrm{d}\boldsymbol{p}_2\mathrm{d}\boldsymbol{p}_3 e^{-\frac{(\boldsymbol{x}'_1-\boldsymbol{x}'_2)^2}{2\sigma_1^2}} e^{-\frac{2(\frac{m_1\boldsymbol{x}'_1}{m_1+m_2}+\frac{m_2\boldsymbol{x}'_2}{m_1+m_2}-\boldsymbol{x}'_3)^2}{3\sigma_2^2}} \\ &\quad f^{(n)}_{\mathrm{h}_1\mathrm{h}_2\mathrm{h}_3}(\boldsymbol{x}_1,\boldsymbol{x}_2,\boldsymbol{x}_3;\boldsymbol{p}_1,\boldsymbol{p}_2,\boldsymbol{p}_3) \\ &\quad \times e^{-\frac{2\sigma_1^2(m_2\boldsymbol{p}'_1-m_1\boldsymbol{p}'_2)^2}{(m_1+m_2)^2}} e^{-\frac{3\sigma_2^2[m_3\boldsymbol{p}'_1+m_3\boldsymbol{p}'_2-(m_1+m_2)\boldsymbol{p}'_3]^2}{2(m_1+m_2+m_3)^2}} \delta\left(\sum_{i=1}^{3}\boldsymbol{p}_i-\boldsymbol{p}\right). \end{aligned} \tag{19}$$

Approximating the Gaussian form of the momentum-dependent kernel function to be a δ function and integrating $\boldsymbol{p}_1$, $\boldsymbol{p}_2$, and $\boldsymbol{p}_3$ from Eq. (19), we obtain

$$\begin{aligned} f_{\mathrm{H}_j}(\boldsymbol{p}) &= 8^2 N_{\mathrm{h}_1\mathrm{h}_2\mathrm{h}_3} g_{\mathrm{H}_j} \int \mathrm{d}\boldsymbol{x}_1\mathrm{d}\boldsymbol{x}_2\mathrm{d}\boldsymbol{x}_3\mathrm{d}\boldsymbol{p}_1 d\boldsymbol{p}_2 d\boldsymbol{p}_3 f^{(n)}_{\mathrm{h}_1\mathrm{h}_2\mathrm{h}_3}(\boldsymbol{x}_1,\boldsymbol{x}_2,\boldsymbol{x}_3;\boldsymbol{p}_1,\boldsymbol{p}_2,\boldsymbol{p}_3) \\ &\quad e^{-\frac{(\boldsymbol{x}'_1-\boldsymbol{x}'_2)^2}{2\sigma_1^2}} e^{-\frac{2\left(\frac{m_1\boldsymbol{x}'_1}{m_1+m_2}+\frac{m_2\boldsymbol{x}'_2}{m_1+m_2}-\boldsymbol{x}'_3\right)^2}{3\sigma_2^2}} \\ &\quad \times\left(\frac{\sqrt{\pi}}{\sqrt{2}\sigma_1}\right)^3\left(1+\frac{m_1}{m_2}\right)^3 \\ &\quad \delta\left(\boldsymbol{p}'_1-\frac{m_1}{m_2}\boldsymbol{p}'_2\right)\left(\frac{\sqrt{2}\pi}{\sqrt{3}\sigma_2}\right)^3\left(1+\frac{m_1}{m_3}+\frac{m_2}{m_3}\right)^3 \\ &\quad \delta\left(\boldsymbol{p}'_1+\boldsymbol{p}'_2-\frac{m_1+m_2}{m_3}\boldsymbol{p}'_3\right)\delta\left(\sum_{i=1}^{3}\boldsymbol{p}_i-\boldsymbol{p}\right) \\ &= 8^2 N_{\mathrm{h}_1\mathrm{h}_2\mathrm{h}_3} g_{\mathrm{H}_j} \int \mathrm{d}\boldsymbol{x}_1\mathrm{d}\boldsymbol{x}_2\mathrm{d}\boldsymbol{x}_3\mathrm{d}\boldsymbol{p}_1\mathrm{d}\boldsymbol{p}_2 d\boldsymbol{p}_3 f^{(n)}_{\mathrm{h}_1\mathrm{h}_2\mathrm{h}_3}(\boldsymbol{x}_1,\boldsymbol{x}_2,\boldsymbol{x}_3;\boldsymbol{p}_1,\boldsymbol{p}_2,\boldsymbol{p}_3) \\ &\quad e^{-\frac{(\boldsymbol{x}'_1-\boldsymbol{x}'_2)^2}{2\sigma_1^2}} e^{-\frac{2\left(\frac{m_1\boldsymbol{x}'_1}{m_1+m_2}+\frac{m_2\boldsymbol{x}'_2}{m_1+m_2}-\boldsymbol{x}'_3\right)^2}{3\sigma_2^2}} \\ &\quad \times\left(\frac{\sqrt{\pi}}{\sqrt{2}\sigma_1}\right)^3\left(1+\frac{m_1}{m_2}\right)^3\gamma\delta\left(\boldsymbol{p}_1-\frac{m_1}{m_2}\boldsymbol{p}_2\right)\left(\frac{\sqrt{2}\pi}{\sqrt{3}\sigma_2}\right)^3 \\ &\quad \left(1+\frac{m_1}{m_3}+\frac{m_2}{m_3}\right)^3 \\ &\quad \gamma\delta\left(\boldsymbol{p}_1+\boldsymbol{p}_2-\frac{m_1+m_2}{m_3}\boldsymbol{p}_3\right)\delta\left(\sum_{i=1}^{3}\boldsymbol{p}_i-\boldsymbol{p}\right) \\ &= 8^2 N_{\mathrm{h}_1\mathrm{h}_2\mathrm{h}_3} g_{\mathrm{H}_j}\gamma^2\left(\frac{\pi}{\sqrt{3}\sigma_1\sigma_2}\right)^3 \\ &\quad \int \mathrm{d}\boldsymbol{x}_1\mathrm{d}\boldsymbol{x}_2\mathrm{d}\boldsymbol{x}_3 f^{(n)}_{\mathrm{h}_1\mathrm{h}_2\mathrm{h}_3}\left(\boldsymbol{x}_1,\boldsymbol{x}_2,\boldsymbol{x}_3;\frac{m_1\boldsymbol{p}}{m_1+m_2+m_3},\right. \\ &\quad \left.\frac{m_2\boldsymbol{p}}{m_1+m_2+m_3},\frac{m_3\boldsymbol{p}}{m_1+m_2+m_3}\right) \\ &\quad \times e^{-\frac{(\boldsymbol{x}'_1-\boldsymbol{x}'_2)^2}{2\sigma_1^2}} e^{-\frac{2\left(\frac{m_1\boldsymbol{x}'_1}{m_1+m_2}+\frac{m_2\boldsymbol{x}'_2}{m_1+m_2}-\boldsymbol{x}'_3\right)^2}{3\sigma_2^2}}. \end{aligned} \tag{20}$$

Changing coordinate variables in Eq. (20) to $\boldsymbol{Y}=(m_1\boldsymbol{x}_1+m_2\boldsymbol{x}_2+m_3\boldsymbol{x}_3)/(m_1+m_2+m_3)$, $\boldsymbol{r}_1=(\boldsymbol{x}_1-\boldsymbol{x}_2)/\sqrt{2}$ and $\boldsymbol{r}_2=\sqrt{\frac{2}{3}}(\frac{m_1\boldsymbol{x}_1}{m_1+m_2}+\frac{m_2\boldsymbol{x}_2}{m_1+m_2}-\boldsymbol{x}_3)$, as reported in Refs. [65–67], we get

$$\begin{aligned} f_{\mathrm{H}_j}(\boldsymbol{p}) &= 8^2 N_{\mathrm{h}_1\mathrm{h}_2\mathrm{h}_3} g_{\mathrm{H}_j}\gamma^2\left(\frac{\pi}{\sqrt{3}\sigma_1\sigma_2}\right)^3 \\ &\quad \times\int 3^{3/2}\mathrm{d}\boldsymbol{Y}\mathrm{d}\boldsymbol{r}_1\mathrm{d}\boldsymbol{r}_2 f^{(n)}_{\mathrm{h}_1\mathrm{h}_2\mathrm{h}_3} \\ &\quad \left(\boldsymbol{Y},\boldsymbol{r}_1,\boldsymbol{r}_2;\frac{m_1\boldsymbol{p}}{m_1+m_2+m_3},\frac{m_2\boldsymbol{p}}{m_1+m_2+m_3},\frac{m_3\boldsymbol{p}}{m_1+m_2+m_3}\right)e^{-\frac{\boldsymbol{r}'^2_1}{\sigma_1^2}}e^{-\frac{\boldsymbol{r}'^2_2}{\sigma_2^2}}. \end{aligned} \tag{21}$$

Assuming the center of mass coordinate in the joint distribution to be factorized gives

$$3^{3/2}f^{(n)}_{\mathrm{h}_1\mathrm{h}_2\mathrm{h}_3}\left(\boldsymbol{Y},\boldsymbol{r}_1,\boldsymbol{r}_2;\frac{m_1\boldsymbol{p}}{m_1+m_2+m_3},\frac{m_2\boldsymbol{p}}{m_1+m_2+m_3},\frac{m_3\boldsymbol{p}}{m_1+m_2+m_3}\right)$$
$$=f^{(n)}_{\mathrm{h}_1\mathrm{h}_2\mathrm{h}_3}(\boldsymbol{Y})f^{(n)}_{\mathrm{h}_1\mathrm{h}_2\mathrm{h}_3}\left(\boldsymbol{r}_1,\boldsymbol{r}_2;\frac{m_1\boldsymbol{p}}{m_1+m_2+m_3},\frac{m_2\boldsymbol{p}}{m_1+m_2+m_3},\frac{m_3\boldsymbol{p}}{m_1+m_2+m_3}\right). \tag{22}$$

Substituting Eq. (22) into Eq. (21), we get

$$f_{\mathrm{H}_j}(\boldsymbol{p})=8^2N_{\mathrm{h}_1\mathrm{h}_2\mathrm{h}_3}g_{\mathrm{H}_j}\gamma^2\left(\frac{\pi}{\sqrt{3}\sigma_1\sigma_2}\right)^3\int \mathrm{d}\boldsymbol{r_1}\mathrm{d}\boldsymbol{r_2}f^{(n)}_{\mathrm{h}_1\mathrm{h}_2\mathrm{h}_3}\left(\boldsymbol{r}_1,\boldsymbol{r}_2;\frac{m_1\boldsymbol{p}}{m_1+m_2+m_3},\frac{m_2\boldsymbol{p}}{m_1+m_2+m_3},\frac{m_3\boldsymbol{p}}{m_1+m_2+m_3}\right)\times e^{-\frac{\boldsymbol{r}_1'^2}{\sigma_1^2}}e^{-\frac{\boldsymbol{r}_2'^2}{\sigma_2^2}}. \tag{23}$$

Adopting the Gaussian forms for the relative coordinate distributions [60, 68–70], we get

$$f^{(n)}_{\mathrm{h}_1\mathrm{h}_2\mathrm{h}_3}\left(\boldsymbol{r}_1,\boldsymbol{r}_2;\frac{m_1\boldsymbol{p}}{m_1+m_2+m_3},\frac{m_2\boldsymbol{p}}{m_1+m_2+m_3},\frac{m_3\boldsymbol{p}}{m_1+m_2+m_3}\right)$$
$$=\frac{1}{[\pi C_1R_\mathrm{f}^2(\boldsymbol{p})]^{3/2}}e^{-\frac{\boldsymbol{r}_1^2}{C_1R_\mathrm{f}^2(\boldsymbol{p})}}\frac{1}{[\pi C_2R_\mathrm{f}^2(\boldsymbol{p})]^{3/2}}e^{-\frac{\boldsymbol{r}_2^2}{C_2R_\mathrm{f}^2(\boldsymbol{p})}}f^{(n)}_{\mathrm{h}_1\mathrm{h}_2\mathrm{h}_3}\left(\frac{m_1\boldsymbol{p}}{m_1+m_2+m_3},\frac{m_2\boldsymbol{p}}{m_1+m_2+m_3},\frac{m_3\boldsymbol{p}}{m_1+m_2+m_3}\right). \tag{24}$$

Comparing the relationships of $\boldsymbol{r}_1$ and $\boldsymbol{r}_2$ with $\boldsymbol{x}_1$, $\boldsymbol{x}_2$, and $\boldsymbol{x}_3$ to that of $\boldsymbol{r}$ with $\boldsymbol{x}_1$ and $\boldsymbol{x}_2$ presented in Sect. 2.1, we observe that C_1 is equal to C_0 and C_2 is $4C_0/3$ [60, 68–70]. Substituting Eq. (24) into Eq. (23) and considering the coordinate Lorentz transformation, we integrate from the relative coordinate variables and obtain

$$f_{\mathrm{H}_j}(\boldsymbol{p})=\frac{8^2\pi^3g_{\mathrm{H}_j}\gamma^2}{3^{3/2}\left[C_1R_\mathrm{f}^2(\boldsymbol{p})+\sigma_1^2\right]\sqrt{C_1[R_\mathrm{f}(\boldsymbol{p})/\gamma]^2+\sigma_1^2}\left[C_2R_\mathrm{f}^2(\boldsymbol{p})+\sigma_2^2\right]\sqrt{C_2[R_\mathrm{f}(\boldsymbol{p})/\gamma]^2+\sigma_2^2}}\times f_{\mathrm{h}_1\mathrm{h}_2\mathrm{h}_3}\left(\frac{m_1\boldsymbol{p}}{m_1+m_2+m_3},\frac{m_2\boldsymbol{p}}{m_1+m_2+m_3},\frac{m_3\boldsymbol{p}}{m_1+m_2+m_3}\right). \tag{25}$$

Ignoring the correlations between h_1, h_2, and h_3, we get the three-dimensional momentum distribution of H_j as

$$f_{\mathrm{H}_j}(\boldsymbol{p})=\frac{8^2\pi^3g_{\mathrm{H}_j}\gamma^2}{3^{3/2}\left[C_1R_\mathrm{f}^2(\boldsymbol{p})+\sigma_1^2\right]\sqrt{C_1[R_\mathrm{f}(\boldsymbol{p})/\gamma]^2+\sigma_1^2}\left[C_2R_\mathrm{f}^2(\boldsymbol{p})+\sigma_2^2\right]\sqrt{C_2[R_\mathrm{f}(\boldsymbol{p})/\gamma]^2+\sigma_2^2}}\times f_{\mathrm{h}_1}\left(\frac{m_1\boldsymbol{p}}{m_1+m_2+m_3}\right)f_{\mathrm{h}_2}\left(\frac{m_2\boldsymbol{p}}{m_1+m_2+m_3}\right)f_{\mathrm{h}_3}\left(\frac{m_3\boldsymbol{p}}{m_1+m_2+m_3}\right). \tag{26}$$

Finally, the Lorentz invariant momentum distribution can be expressed as

$$f^{(\mathrm{inv})}_{\mathrm{H}_j}(p_\mathrm{T},y)=\frac{8^2\pi^3g_{\mathrm{H}_j}}{3^{3/2}\left[C_1R_\mathrm{f}^2(p_\mathrm{T},y)+\sigma_1^2\right]\sqrt{C_1[R_\mathrm{f}(p_\mathrm{T},y)/\gamma]^2+\sigma_1^2}\left[C_2R_\mathrm{f}^2(p_\mathrm{T},y)+\sigma_2^2\right]\sqrt{C_2[R_\mathrm{f}(p_\mathrm{T},y)/\gamma]^2+\sigma_2^2}}\times\frac{m_{\mathrm{H}_j}}{m_1m_2m_3}f^{(\mathrm{inv})}_{\mathrm{h}_1}(\frac{m_1p_\mathrm{T}}{m_1+m_2+m_3},y)f^{(\mathrm{inv})}_{\mathrm{h}_2}(\frac{m_2p_\mathrm{T}}{m_1+m_2+m_3},y)\,f^{(\mathrm{inv})}_{\mathrm{h}_3}(\frac{m_3p_\mathrm{T}}{m_1+m_2+m_3},y). \tag{27}$$

In summary, Eqs. (15) and (27) give the following: (i) the relationships of dibaryon states and tribaryon states with primordial baryons in momentum space in a laboratory frame, (ii) effects of different factors on dibaryon or tribaryon production; e.g., the whole hadronic system scale and the size of the formed composite object. These equations can be directly used to calculate the production of light nuclei, hypernuclei, and even other hadronic molecular states. Moreover, they can be conveniently used to investigate production correlations of different species of composite objects. As the formulae for the antiparticles are the same as those for the dibaryon and tribaryon states, we have not derived them here to eliminate duplication. Their applications at midrapidity (i.e., $y = 0$) in heavy ion collisions at the LHC are presented in the following sections.

3 Results of light nuclei

This section presents the use of the coalescence model to study productions of d, $^3\overline{\mathrm{He}}$ and $\bar{\mathrm{t}}$ at midrapidity in Pb+Pb collisions at $\sqrt{s_{\mathrm{NN}}} = 5.02\,\mathrm{TeV}$. First, we calculate the coalescence factors B_2 and B_3 and discuss their centrality and p_T-dependent behaviors. Subsequently, we compute the p_T spectra of d, $^3\overline{\mathrm{He}}$, and $\bar{\mathrm{t}}$. Finally, we calculate the averaged transverse momenta $\langle p_\mathrm{T}\rangle$, the yield rapidity densities $\mathrm{d}N/\mathrm{d}y$, and the yield ratios of different light nuclei.

3.1 Coalescence factor of light nuclei

The coalescence factor B_A is defined as

$$B_A(p_\mathrm{T}) = \frac{f^{(\mathrm{inv})}_{\mathrm{d},^3\mathrm{He},\mathrm{t}}(p_\mathrm{T})}{\left[f^{(\mathrm{inv})}_{\mathrm{p}}(\frac{p_\mathrm{T}}{A})\right]^Z \left[f^{(\mathrm{inv})}_{\mathrm{n}}(\frac{p_\mathrm{T}}{A})\right]^{A-Z}}, \tag{28}$$

where A is the mass number and Z is the charge of the light nuclei. It is a unique link between the formed light nuclei and the primordial nucleons. Several studies have investigated B_A using different coalescence models [72–75]. From Eqs. (15) and (27), we get for d, ^{3}He, and t, as follows:

$$B_2(p_\mathrm{T}) = \frac{m_\mathrm{d} g_\mathrm{d} (\sqrt{2\pi})^3}{m_\mathrm{p} m_\mathrm{n} \left[C_0 R_\mathrm{f}^2(p_\mathrm{T}) + \sigma_\mathrm{d}^2\right] \sqrt{C_0 [\frac{R_\mathrm{f}(p_\mathrm{T})}{\gamma}]^2 + \sigma_\mathrm{d}^2}}, \tag{29}$$

$$B_3(p_\mathrm{T}) = \frac{64\pi^3 g_{^3\mathrm{He}}}{3^{\frac{3}{2}} \left[C_1 R_\mathrm{f}^2(p_\mathrm{T}) + \sigma_{^3\mathrm{He}}^2\right] \sqrt{C_1 [\frac{R_\mathrm{f}(p_\mathrm{T})}{\gamma}]^2 + \sigma_{^3\mathrm{He}}^2}} \times \frac{m_{^3\mathrm{He}}}{m_\mathrm{p}^2 m_\mathrm{n} \left[C_2 R_\mathrm{f}^2(p_\mathrm{T}) + \sigma_{^3\mathrm{He}}^2\right] \sqrt{C_2 [\frac{R_\mathrm{f}(p_\mathrm{T})}{\gamma}]^2 + \sigma_{^3\mathrm{He}}^2}}, \tag{30}$$

$$B_3(p_\mathrm{T}) = \frac{64\pi^3 g_\mathrm{t}}{3^{\frac{3}{2}} \left[C_1 R_\mathrm{f}^2(p_\mathrm{T}) + \sigma_\mathrm{t}^2\right] \sqrt{C_1 [\frac{R_\mathrm{f}(p_\mathrm{T})}{\gamma}]^2 + \sigma_\mathrm{t}^2}} \times \frac{m_\mathrm{t}}{m_\mathrm{p} m_\mathrm{n}^2 \left[C_2 R_\mathrm{f}^2(p_\mathrm{T}) + \sigma_\mathrm{t}^2\right] \sqrt{C_2 [\frac{R_\mathrm{f}(p_\mathrm{T})}{\gamma}]^2 + \sigma_\mathrm{t}^2}}. \tag{31}$$

Here, $\sigma_\mathrm{d} = \sqrt{\frac{4}{3}} R_\mathrm{d}$, and the root-mean-square radius of the deuteron $R_\mathrm{d} = 2.1421\,\mathrm{fm}$ [76]. Moreover, $\sigma_{^3\mathrm{He}} = R_{^3\mathrm{He}} = 1.9661\,\mathrm{fm}$, $\sigma_\mathrm{t} = R_\mathrm{t} = 1.7591\,\mathrm{fm}$ [76], $m_{\mathrm{p,n}}$ denotes the nucleon mass, and $m_{\mathrm{d},^3\mathrm{He},\mathrm{t}}$ denotes the mass of the d, ^{3}He, or t, respectively.

To further compute B_2 and B_3, the specific form of $R_\mathrm{f}(p_\mathrm{T})$ is necessary. Similar to Ref. [61], the dependence of $R_\mathrm{f}(p_\mathrm{T})$ on centrality and p_T is considered to factorize into a linear

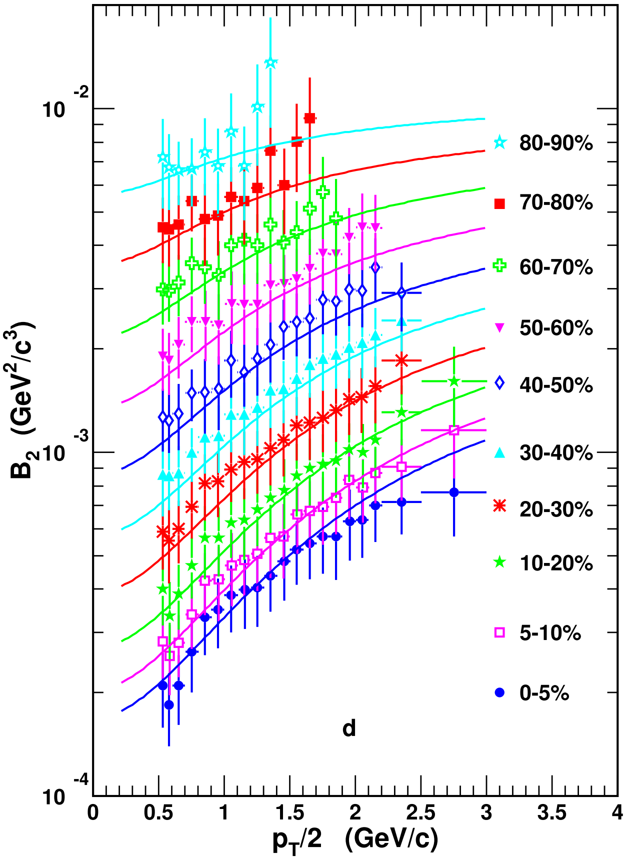

Fig. 1 (Color online) B_2 of d as a function of $p_\mathrm{T}/2$ in different centralities in Pb+Pb collisions at $\sqrt{s_{\mathrm{NN}}} = 5.02\,\mathrm{TeV}$. Symbols with error bars represent experimental data [77], and solid lines represent theoretical results

dependence on the cube root of the pseudorapidity density of charged particles $(\mathrm{d}N_{\mathrm{ch}}/\mathrm{d}\eta)^{1/3}$ and a power-law dependence on the transverse mass of the formed light nucleus [70]. Therefore, we get

$$R_{\mathrm{f}}(p_{\mathrm{T}}) = a \times (\mathrm{d}N_{\mathrm{ch}}/\mathrm{d}\eta)^{\frac{1}{3}} \times \left(\sqrt{p_{\mathrm{T}}^2 + m^2_{\mathrm{d},^3\mathrm{He},\mathrm{t}}}\right)^b, \qquad (32)$$

where a and b are the free parameters, and their values in Pb+Pb collisions at $\sqrt{s_{\mathrm{NN}}} = 5.02\,\mathrm{TeV}$ are (0.70, −0.31) for d and (0.66, −0.31) for $^3\mathrm{He}$ and t, determined by reproducing the experimental data of p_{T} spectra of d and $^3\mathrm{He}$ in the most central 0–5% centrality. Here, b is set to be centrality-independent and is consistent with that in hydrodynamics [78] and that in STAR measurements of two-pion interferometry in central and semi-central Au+Au collisions [79]. Moreover, a is set to be centrality-independent, the same as that in our previous work [61].

We used the data of $\mathrm{d}N_{\mathrm{ch}}/\mathrm{d}\eta$ reported in Ref. [80] to evaluate $R_{\mathrm{f}}(p_{\mathrm{T}})$ and computed the coalescence factors B_2 and B_3. Figure 1 shows B_2 of d as a function of the transverse momentum scaled by the mass number $p_{\mathrm{T}}/2$ in different centralities in Pb+Pb collisions at $\sqrt{s_{\mathrm{NN}}} = 5.02\,\mathrm{TeV}$. Symbols with error bars represent experimental data [77], and solid lines represent theoretical results of the coalescence model. As observed from Fig. 1, from central to peripheral collisions, B_2 exhibits an increasing trend owing to the decreasing scale of the created hadronic system. For a certain centrality, B_2 increases as a function of $p_{\mathrm{T}}/2$. This increased behavior results, on the one hand, from the Lorentz contraction factor γ, which has been studied in Ref. [60]. On the other hand, it results from the decreasing R_{f} with increasing p_{T}. The increase in the experimental data as a function of $p_{\mathrm{T}}/2$ from central to peripheral collisions can be quantitatively described by the coalescence model.

Figure 2 shows B_3 of $^3\overline{\mathrm{He}}$ and that of $\bar{\mathrm{t}}$ as a function of $p_{\mathrm{T}}/3$ in different centralities in Pb+Pb collisions at $\sqrt{s_{\mathrm{NN}}} = 5.02\,\mathrm{TeV}$. Symbols with error bars represent experimental data [62], and solid lines represent theoretical results. Similar to B_2, the experimental data of B_3 exhibit an increasing trend as a function of $p_{\mathrm{T}}/3$ and is reproduced well by the coalescence model from central to peripheral collisions. Figures 1 and 2 show that the centrality and p_{T}-dependent behaviors of B_2 and B_3 are simultaneously explained by the coalescence model. The results extracted for $R_{\mathrm{f}}(p_{\mathrm{T}})$ can provide quantitative references for future measurements of HBT interferometry radius from the two-nucleon correlations. Through the light nucleus production, we provide an alternative way to obtain the HBT interferometry radius of the hadronic source system.

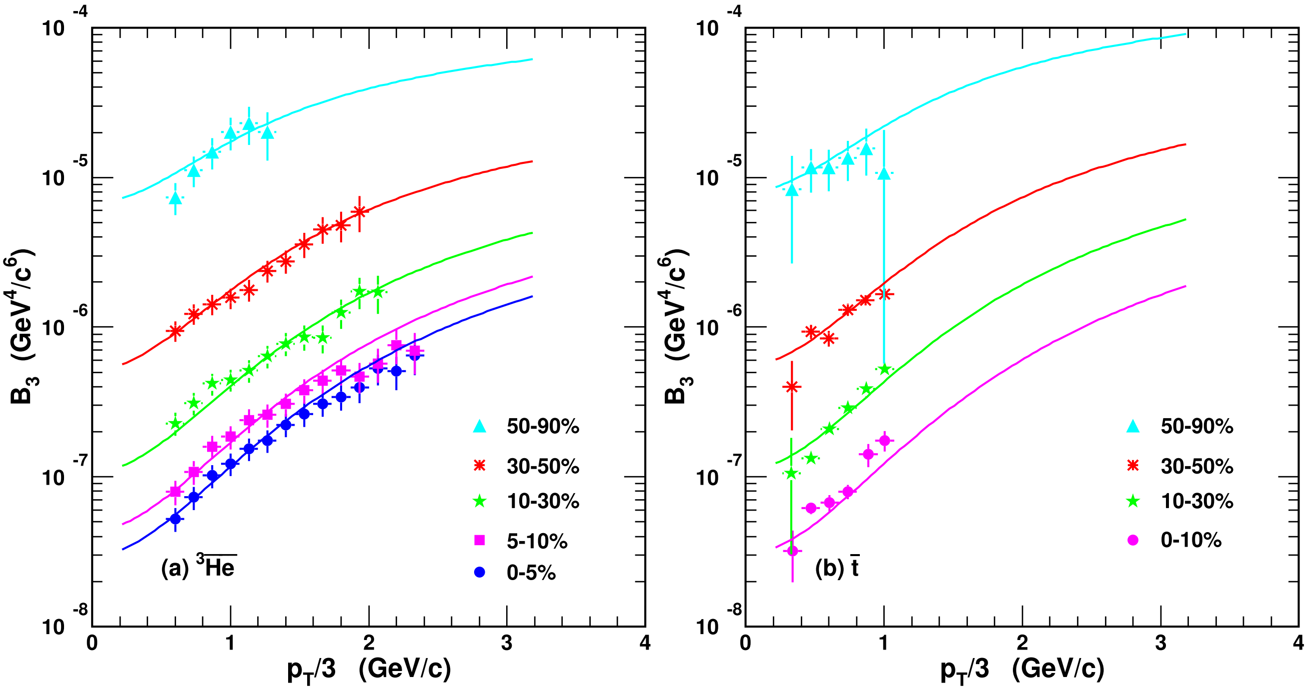

Fig. 2 (Color online) B_3 of (**a**) $^3\overline{\mathrm{He}}$ and (**b**) $\bar{\mathrm{t}}$ as a function of $p_{\mathrm{T}}/3$ in different centralities in Pb+Pb collisions at $\sqrt{s_{\mathrm{NN}}} = 5.02\,\mathrm{TeV}$. Symbols with error bars represent experimental data [62], and solid lines represent theoretical results

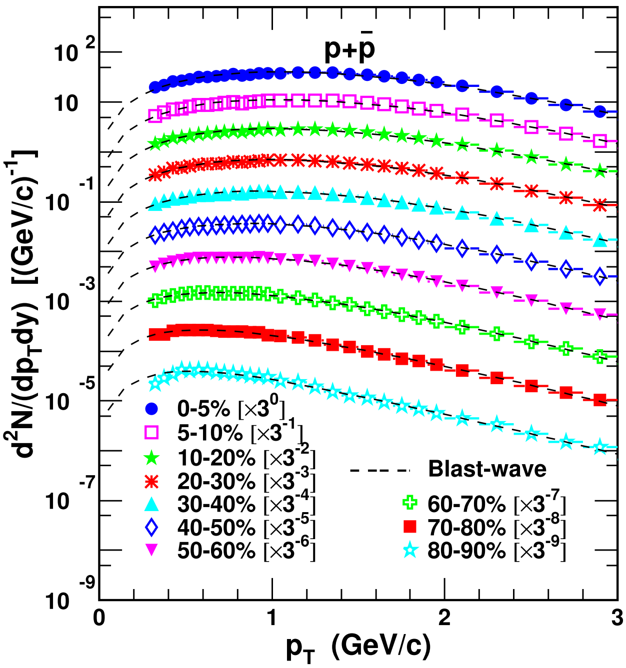

Fig. 3 (Color online) p_T spectra of prompt protons plus antiprotons in different centralities in Pb+Pb collisions at $\sqrt{s_{NN}} = 5.02$ TeV. Symbols with error bars represent experimental data [80], and dashed lines represent the results of the blast-wave model

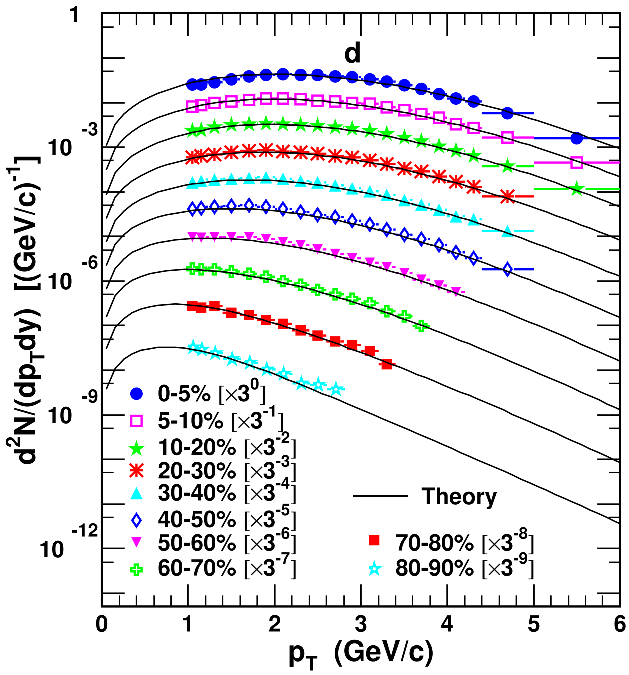

Fig. 4 (Color online) p_T spectra of deuterons in different centralities in Pb+Pb collisions at $\sqrt{s_{NN}} = 5.02$ TeV. Symbols with error bars represent experimental data [77], and solid lines represent the theoretical results

3.2 p_T spectra of light nuclei

The p_T spectra of primordial nucleons are necessary inputs for computing p_T distributions of light nuclei in the coalescence model. Here, we used the blast-wave model to get p_T distribution functions of primordial protons by fitting the experimental data of prompt (anti)protons, as reported in Ref. [80]. The blast-wave function [81] is given as

$$\frac{\mathrm{d}^2N}{2\pi p_T \mathrm{d}p_T \mathrm{d}y} \propto \int_0^R r\mathrm{d}r m_T I_0\left(\frac{p_T \sinh\rho}{T_{\mathrm{kin}}}\right) K_1\left(\frac{m_T \cosh\rho}{T_{\mathrm{kin}}}\right), \tag{33}$$

where r is the radial distance in the transverse plane and R is the fireball radius. Moreover, I_0 and K_1 are the modified Bessel functions, and the velocity profile $\rho = \tanh^{-1}\beta_T = \tanh^{-1}[\beta_s(\frac{r}{R})^n]$. The kinetic freeze-out temperature T_{kin}, the averaged radial expansion velocity $\langle\beta_T\rangle$, and n are fit parameters. Their values can be found in Ref. [80].

Figure 3 shows the p_T spectra of prompt protons plus antiprotons in different centralities in Pb+Pb collisions at $\sqrt{s_{NN}} = 5.02$ TeV. Symbols with error bars represent experimental data [80], and dashed lines represent the results of the blast-wave model. The p_T spectra in different centralities are scaled by different factors for clarity, as shown in Fig. 3. For the primordial neutrons, we adopted the same p_T spectra as those of primordial protons, as we focused on light nucleus production at midrapidity at high LHC energy, that the isospin symmetry was well satisfied.

First, the p_T spectra of deuterons in Pb+Pb collisions at $\sqrt{s_{NN}} = 5.02$ TeV in 0–5%, 5–10%, 10–20%, 20–30%, 30–40%, 40–50%, 50–60%, 60–70%, 70–80%, and 80–90% centralities are calculated. Different solid lines scaled by different factors for clarity in Fig. 4 represent our theoretical results. Symbols with error bars represent the experimental data from the ALICE collaboration [62]. Subsequently, the p_T spectra of $^3\overline{\mathrm{He}}$ and $\bar{\mathrm{t}}$ in Pb+Pb collisions at $\sqrt{s_{NN}} = 5.02$ TeV in different centralities are computed. Different solid lines in Fig. 5 represent our theoretical results, which agree with the available data denoted by the filled symbols [62]. As observed from Figs. 4 and 5, nucleon coalescence is the dominant mechanism for light nucleus production in Pb+Pb collisions at $\sqrt{s_{NN}} = 5.02$ TeV. More precise measurements for $^3\overline{\mathrm{He}}$ and $\bar{\mathrm{t}}$ in a wide p_T range in the future can help test the coalescence mechanism further, specifically in peripheral Pb+Pb collisions.

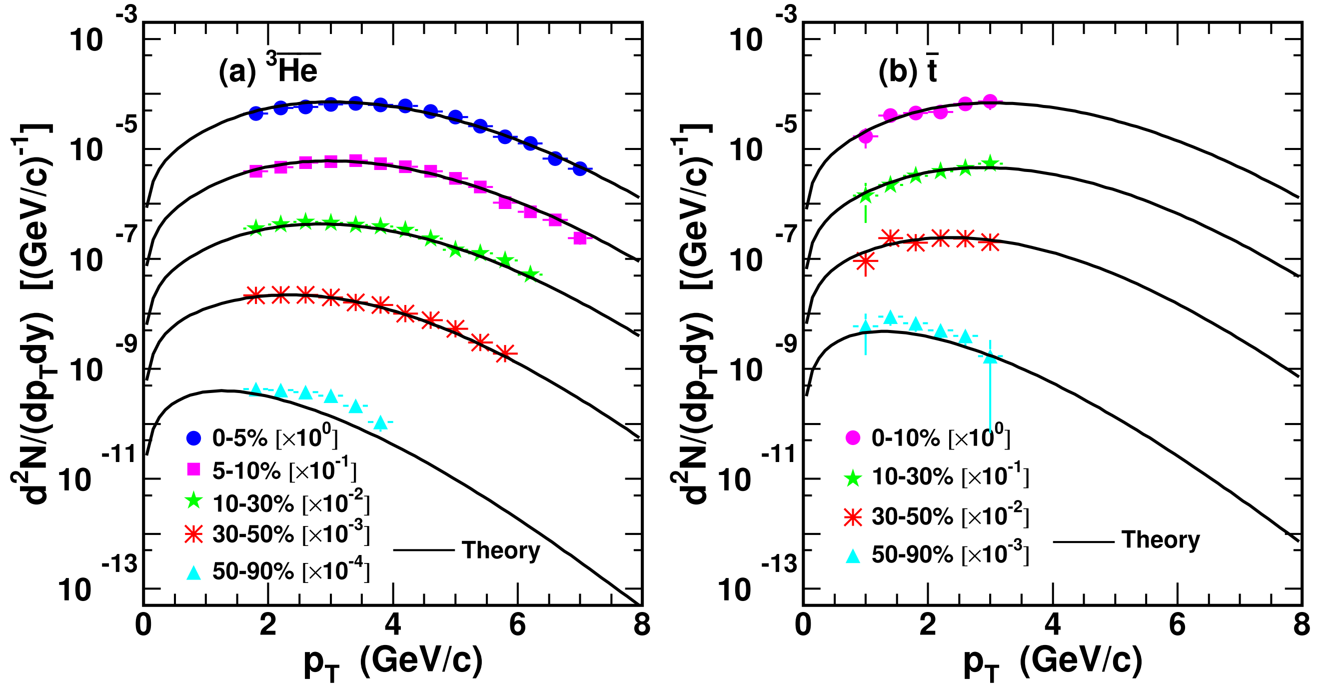

Fig. 5 (Color online) p_T spectra of (**a**) $^3\overline{\mathrm{He}}$ and (**b**) $\bar{\mathrm{t}}$ in different centralities in Pb+Pb collisions at $\sqrt{s_{NN}} = 5.02$ TeV. Filled symbols with error bars represent experimental data [62], and solid lines represent theoretical results

Table 1 Averaged transverse momenta $\langle p_T \rangle$ and yield rapidity densities dN/dy of d, $^3\overline{\mathrm{He}}$, and $\bar{\mathrm{t}}$ in different centralities in Pb+Pb collisions at $\sqrt{s_{NN}} = 5.02$ TeV. Experimental data in the third and fifth columns are obtained from Refs. [62, 77]. Theoretical results are presented in the fourth and sixth columns

	Centrality	$\langle p_T \rangle$ (GeV/c)		dN/dy	
		Data	Theory	Data	Theory
d	0–5%	$2.45 \pm 0.00 \pm 0.09$	2.37	$(1.19 \pm 0.00 \pm 0.21) \times 10^{-1}$	1.22×10^{-1}
	5–10%	$2.41 \pm 0.01 \pm 0.10$	2.33	$(1.04 \pm 0.00 \pm 0.19) \times 10^{-1}$	1.01×10^{-1}
	10–20%	$2.34 \pm 0.00 \pm 0.11$	2.28	$(8.42 \pm 0.02 \pm 1.50) \times 10^{-2}$	7.86×10^{-2}
	20–30%	$2.21 \pm 0.00 \pm 0.12$	2.18	$(6.16 \pm 0.02 \pm 1.10) \times 10^{-2}$	5.58×10^{-2}
	30–40%	$2.05 \pm 0.00 \pm 0.12$	2.04	$(4.25 \pm 0.01 \pm 0.75) \times 10^{-2}$	3.82×10^{-2}
	40–50%	$1.88 \pm 0.01 \pm 0.12$	1.87	$(2.73 \pm 0.01 \pm 0.48) \times 10^{-2}$	2.46×10^{-2}
	50–60%	$1.70 \pm 0.01 \pm 0.11$	1.66	$(1.62 \pm 0.01 \pm 0.28) \times 10^{-2}$	1.47×10^{-2}
	60–70%	$1.46 \pm 0.01 \pm 0.12$	1.45	$(8.35 \pm 0.14 \pm 1.43) \times 10^{-3}$	7.58×10^{-3}
	70–80%	$1.27 \pm 0.02 \pm 0.11$	1.25	$(3.52 \pm 0.06 \pm 0.63) \times 10^{-3}$	3.22×10^{-3}
	80–90%	$1.09 \pm 0.02 \pm 0.40$	1.10	$(1.13 \pm 0.03 \pm 0.23) \times 10^{-3}$	0.925×10^{-3}
$^3\overline{\mathrm{He}}$	0–5%	$3.465 \pm 0.013 \pm 0.154 \pm 0.144$	3.26	$(24.70 \pm 0.28 \pm 2.29 \pm 0.30) \times 10^{-5}$	25.6×10^{-5}
	5–10%	$3.368 \pm 0.014 \pm 0.141 \pm 0.132$	3.21	$(20.87 \pm 0.26 \pm 1.95 \pm 0.43) \times 10^{-5}$	21.4×10^{-5}
	10–30%	$3.237 \pm 0.021 \pm 0.157 \pm 0.150$	3.08	$(15.94 \pm 0.31 \pm 1.53 \pm 0.34) \times 10^{-5}$	14.8×10^{-5}
	30–50%	$2.658 \pm 0.016 \pm 0.084 \pm 0.049$	2.64	$(7.56 \pm 0.13 \pm 0.70 \pm 0.10) \times 10^{-5}$	7.16×10^{-5}
	50–90%	$2.057 \pm 0.023 \pm 0.090 \pm 0.027$	1.77	$(1.19 \pm 0.08 \pm 0.16 \pm 0.14) \times 10^{-5}$	0.931×10^{-5}
$\bar{\mathrm{t}}$	0–10%	$3.368 \pm 0.241 \pm 0.060$	3.27	$(24.45 \pm 1.75 \pm 2.71) \times 10^{-5}$	24.6×10^{-5}
	10–30%	$3.015 \pm 0.286 \pm 0.040$	3.11	$(14.19 \pm 1.35 \pm 1.29) \times 10^{-5}$	15.9×10^{-5}
	30–50%	$2.524 \pm 0.593 \pm 0.180$	2.68	$(7.24 \pm 1.70 \pm 0.65) \times 10^{-5}$	7.97×10^{-5}
	50–90%	$1.636 \pm 0.226 \pm 0.040$	1.80	$(1.66 \pm 0.23 \pm 0.16) \times 10^{-5}$	1.14×10^{-5}

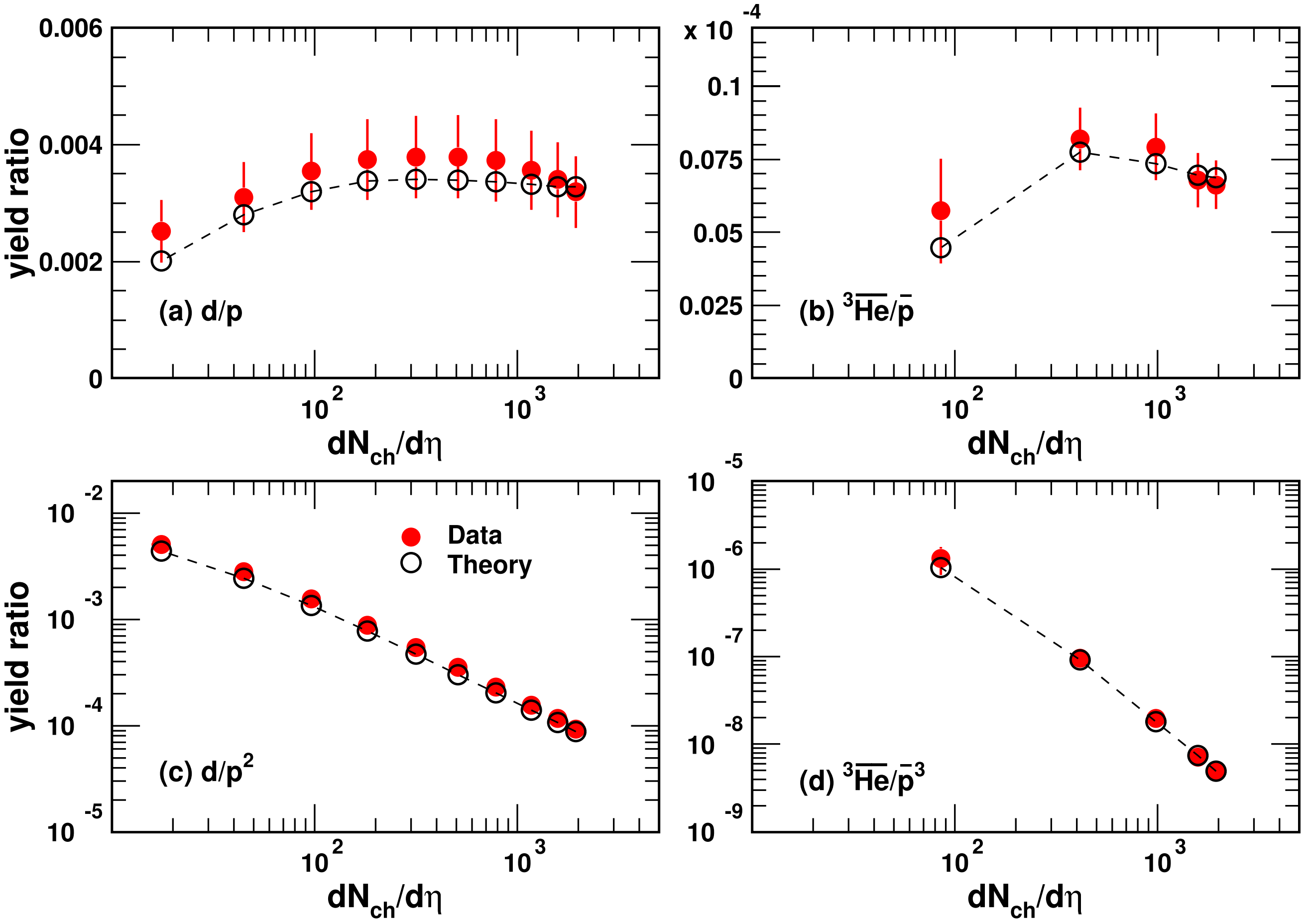

Fig. 6 (Color online) Yield ratios (**a**) d/p, (**b**) $^3\overline{\mathrm{He}}/\bar{\mathrm{p}}$, (**c**) d/p^2, and (**d**) $^3\overline{\mathrm{He}}/\bar{\mathrm{p}}^3$ as a function of dN_{ch}/dη in Pb+Pb collisions at $\sqrt{s_{\mathrm{NN}}} = 5.02$ TeV. Filled circles with error bars represent experimental data [62, 77], and open circles connected with dashed lines to guide the eye represent the theoretical results

3.3 Averaged transverse momenta and yield rapidity densities of light nuclei

The averaged transverse momenta $\langle p_{\mathrm{T}}\rangle$ and yield rapidity densities dN/dy of d, $^3\overline{\mathrm{He}}$, and $\bar{\mathrm{t}}$ are studied. Our theoretical results are presented in the fourth and sixth columns in Table 1. Experimental data presented in the third and fifth columns are obtained from Refs. [62, 77]. A decreasing trend for $\langle p_{\mathrm{T}}\rangle$ and dN/dy from central to peripheral collisions is observed. This is because in collisions that are more central, more energy is deposited in the midrapidity region, and collective evolution exists for longer. Theoretical results for d, $^3\overline{\mathrm{He}}$, and $\bar{\mathrm{t}}$ are consistent with the corresponding data within the experimental uncertainties, except for a very little underestimation for dN/dy of $\bar{\mathrm{t}}$ in a peripheral 50–90% collision. Such underestimation needs to be confirmed using precise data from future research.

3.4 Yield ratios of light nuclei

Yield ratios carry information on the intrinsic production correlations of different light nuclei and are predicted to exhibit nontrivial behaviors [61]. This subsection presents the centrality dependence of different yield ratios, such as d/p, $^3\overline{\mathrm{He}}/\bar{\mathrm{p}}$, d/p^2, $^3\overline{\mathrm{He}}/\bar{\mathrm{p}}^3$, and $\bar{\mathrm{t}}/^3\overline{\mathrm{He}}$.

Figure 6(a) and (b) shows the dN_{ch}/dη dependence of d/p and $^3\overline{\mathrm{He}}/\bar{\mathrm{p}}$ in Pb+Pb collisions at $\sqrt{s_{\mathrm{NN}}} = 5.02$ TeV. Filled circles with error bars represent experimental data [82], and open circles connected with dashed lines to guide the eye represent the theoretical results. From Eq. (15), we approximately obtain the p_{T}-integrated yield ratio as

$$\frac{\mathrm{d}}{\mathrm{p}} \propto \frac{N_{\mathrm{p}}}{\langle R_{\mathrm{f}}\rangle^3\left(C_0+\frac{\sigma_{\mathrm{d}}^2}{\langle R_{\mathrm{f}}\rangle^2}\right)\sqrt{\frac{C_0}{\langle\gamma\rangle^2}+\frac{\sigma_{\mathrm{d}}^2}{\langle R_{\mathrm{f}}\rangle^2}}} = \frac{N_{\mathrm{p}}}{\langle R_{\mathrm{f}}\rangle^3/\langle\gamma\rangle} \times \frac{1}{\left(C_0+\frac{\sigma_{\mathrm{d}}^2}{\langle R_{\mathrm{f}}\rangle^2}\right)\sqrt{C_0+\frac{\sigma_{\mathrm{d}}^2}{\langle R_{\mathrm{f}}\rangle^2/\langle\gamma\rangle^2}}}, \tag{34}$$

where the angle brackets denote the averaged values. Equation (34) implies that the behavior of d/p is determined by two factors—one is the nucleon number density $\frac{N_{\mathrm{p}}}{\langle R_{\mathrm{f}}\rangle^3/\langle\gamma\rangle}$, and the other is the suppression effect from the relative size of the d to the hadronic source system $\frac{\sigma_{\mathrm{d}}}{\langle R_{\mathrm{f}}\rangle}$. Similar case holds for $^3\overline{\mathrm{He}}/\bar{\mathrm{p}}$. The nucleon number density decreases, specifically from semi-central to central collisions [80], thereby decreasing d/p and $^3\overline{\mathrm{He}}/\bar{\mathrm{p}}$ with increasing $\mathrm{d}N_{\mathrm{ch}}/\mathrm{d}\eta$. The relative size $\frac{\sigma_{\mathrm{d}}}{\langle R_{\mathrm{f}}\rangle}$ decreases and its suppression effect becomes weak in large hadronic systems, thereby increasing d/p and $^3\overline{\mathrm{He}}/\bar{\mathrm{p}}$ with increasing $\mathrm{d}N_{\mathrm{ch}}/\mathrm{d}\eta$ [83]. For significantly high $\mathrm{d}N_{\mathrm{ch}}/\mathrm{d}\eta$ area values, the difference in the suppression extents in different centralities becomes insignificant, and the decreasing nucleon number density dominates the decreasing behavior of d/p and $^3\overline{\mathrm{He}}/\bar{\mathrm{p}}$. For low $\mathrm{d}N_{\mathrm{ch}}/\mathrm{d}\eta$ area values, different suppression extents of the relative size in different centralities increase d/p and $^3\overline{\mathrm{He}}/\bar{\mathrm{p}}$ as a function of $\mathrm{d}N_{\mathrm{ch}}/\mathrm{d}\eta$. The final conjunct result from the nucleon number density and the suppression effect first increases d/p and $^3\overline{\mathrm{He}}/\bar{\mathrm{p}}$ from peripheral to semi-central collisions and then decreases them from semi-central to central collisions, as shown in Fig. 6(a) and (b).

Figure 6(c) and (d) shows d/p^2 and $^3\overline{\mathrm{He}}/\bar{\mathrm{p}}^3$ as a function of $\mathrm{d}N_{\mathrm{ch}}/\mathrm{d}\eta$ in Pb+Pb collisions at $\sqrt{s_{\mathrm{NN}}} = 5.02$ TeV. Filled circles with error bars represent experimental data

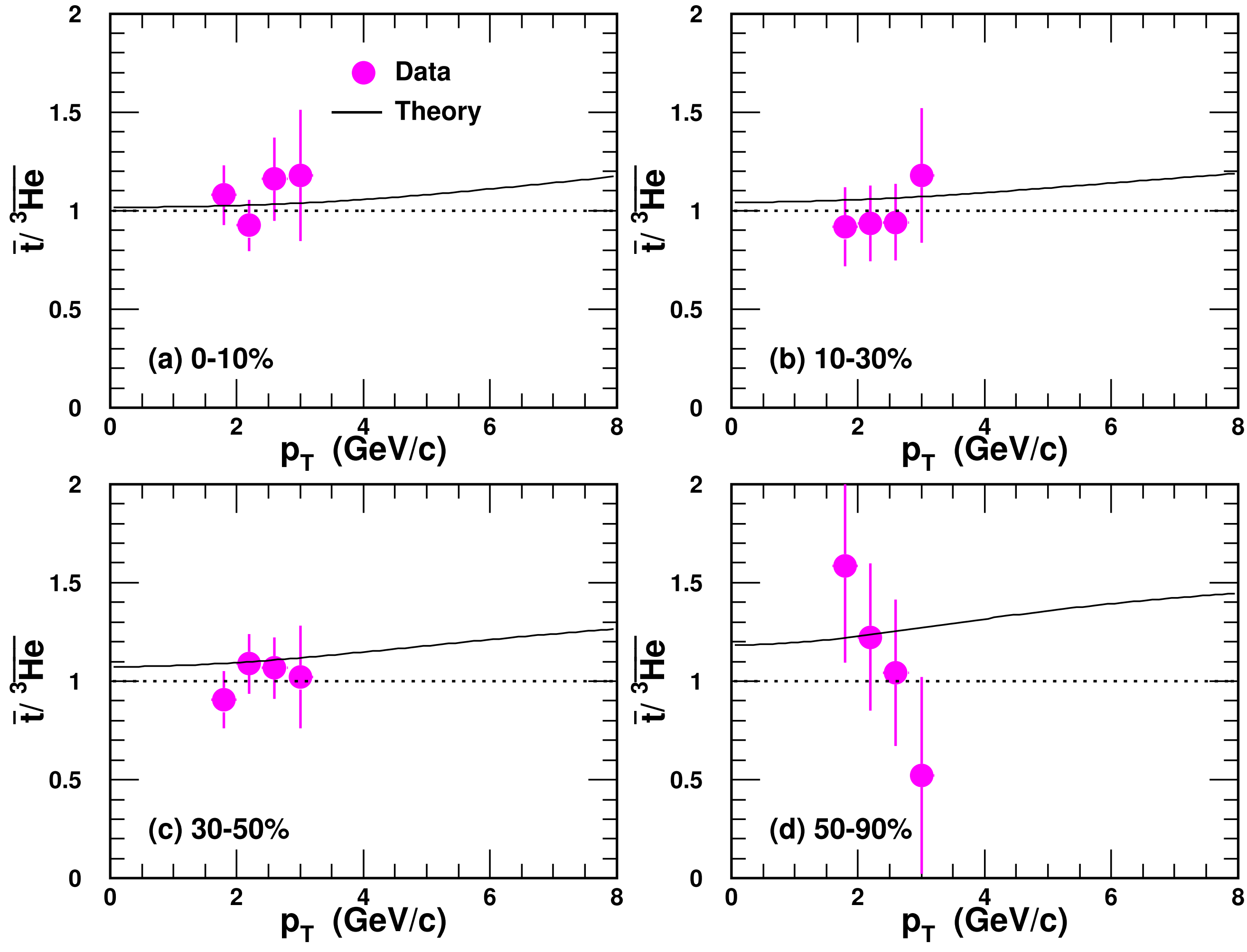

Fig. 7 (Color online) Yield ratio $\bar{\mathrm{t}}/^3\overline{\mathrm{He}}$ as a function of p_{T} in different centralities in Pb+Pb collisions at $\sqrt{s_{\mathrm{NN}}} = 5.02$ TeV. Filled circles with error bars represent experimental data [62], and solid lines represent the theoretical results

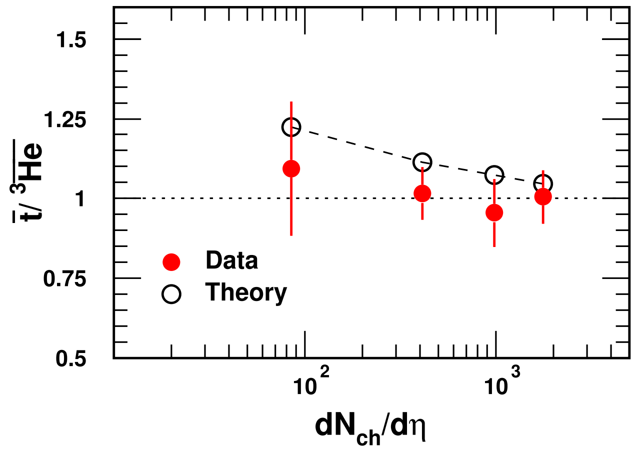

Fig. 8 (Color online) Yield ratio $\bar{\mathrm{t}}/{}^3\overline{\mathrm{He}}$ as a function of $\mathrm{d}N_{\mathrm{ch}}/\mathrm{d}\eta$ in Pb+Pb collisions at $\sqrt{s_{\mathrm{NN}}} = 5.02$ TeV. Filled circles with error bars represent experimental data [62], and open circles connected with dashed lines to guide the eye represent the theoretical results

[82]. Open circles connected with dashed lines to guide the eye represent the theoretical results. Evidently, both graphs exhibit explicit decreasing trends with the increasing $\mathrm{d}N_{\mathrm{ch}}/\mathrm{d}\eta$ and are very different from the previous trends observed for d/p and ${}^3\overline{\mathrm{He}}/\mathrm{p}$. As d/p^2 and ${}^3\overline{\mathrm{He}}/\bar{\mathrm{p}}^3$ represent the probability of any pn-pair coalescing into a deuteron and that of any $\bar{\mathrm{p}}\bar{\mathrm{p}}\bar{\mathrm{n}}$-cluster coalescing into a ${}^3\overline{\mathrm{He}}$, respectively, it is more difficult for any pn-pair or $\bar{\mathrm{p}}\bar{\mathrm{p}}\bar{\mathrm{n}}$-cluster to recombine into a deuteron or ${}^3\overline{\mathrm{He}}$ in the larger hadronic system produced in a more central collision.

Therefore, a yield ratio $\mathrm{t}/{}^3\mathrm{He}$ is proposed as a valuable probe to distinguish the thermal and coalescence productions for light nuclei [61]. In the coalescence framework, the ratio is always greater than one and approaches one at large R_{f} values, where the suppression effect from the nucleus size can be ignored. The smaller the R_{f} value, the higher the deviation of $\mathrm{t}/{}^3\mathrm{He}$ from one. The same case holds for $\bar{\mathrm{t}}/{}^3\overline{\mathrm{He}}$. Figure 7 shows $\bar{\mathrm{t}}/{}^3\overline{\mathrm{He}}$ as a function of p_{T} in Pb+Pb collisions at $\sqrt{s_{\mathrm{NN}}} = 5.02$ TeV in different centralities 0–10%, 10–30%, 30–50%, and 50–90%. Filled circles with error bars represent experimental data [62], and solid lines represent the theoretical results. A reference line of one is plotted as a dotted line. With the increasing p_{T}, R_{f} decreases; consequently, our theoretical results increase. However, this trend is different from that observed in the thermal model, where the expectation for this ratio is one [43]. The trend of the data in 0–10%, 10–30%, and 30–50% centralities is increasing, but a final conclusion is hard to make owing to the limited p_{T} range and the large error bars. Data in the peripheral 50–90% centrality seem to decrease, but further, more

Table 2 Values of parameters in the blast-wave model for Λ and Ω^- in different centralities in Pb+Pb collisions at $\sqrt{s_{\mathrm{NN}}} = 5.02$ TeV

	Centrality	T_{kin} (GeV)	$\langle \beta_{\mathrm{T}} \rangle$	n
Λ	0–10%	0.090	0.670	0.64
	10–30%	0.092	0.648	0.70
	30–50%	0.095	0.622	0.78
Ω^-	0–10%	0.095	0.627	0.78
	10–30%	0.097	0.569	1.05
	30–50%	0.100	0.549	1.15

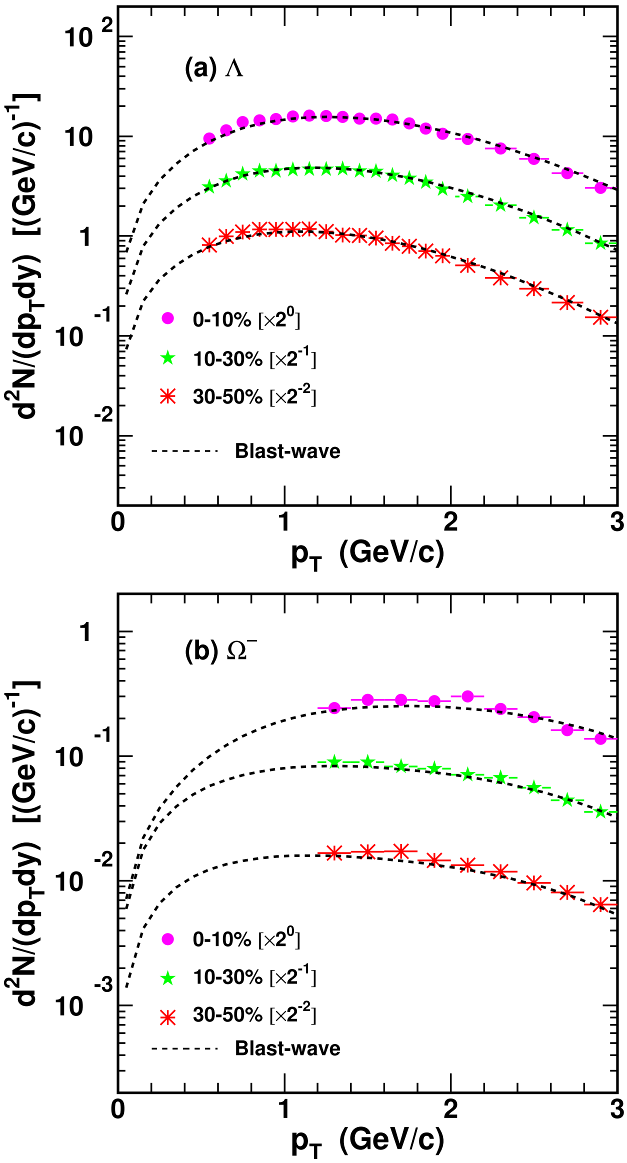

Fig. 9 (Color online) p_{T} spectra of **(a)** Λ and **(b)** Ω^- in different centralities in Pb+Pb collisions at $\sqrt{s_{\mathrm{NN}}} = 5.02$ TeV. Symbols with error bars represent experimental data [84], and dashed lines represent the results of the blast-wave model

precise measurements are needed to confirm this trend. More precise data must be obtained in the future to further distinguish the production mechanisms of $^3\overline{\text{He}}$ and $\bar{\text{t}}$.

The p_T-integrated yield ratio $\bar{\text{t}}/^3\overline{\text{He}}$ as a function of $\mathrm{d}N_{\mathrm{ch}}/\mathrm{d}\eta$ is shown in Fig. 8. Filled circles with error bars represent experimental data [62], and open circles connected with the dashed line to guide the eye represent the theoretical results. A reference line of one is also plotted as a dotted line. Here, $\bar{\text{t}}/^3\overline{\text{He}}$ exhibits a decreasing trend. This is because of the larger $\mathrm{d}N_{\mathrm{ch}}/\mathrm{d}\eta$ values, i.e., the larger R_f values decreases $\bar{\text{t}}/^3\overline{\text{He}}$ to be closer to one. Theoretical results of $\bar{\text{t}}/^3\overline{\text{He}}$ in the coalescence model show a non-flat behavior as a function of $\mathrm{d}N_{\mathrm{ch}}/\mathrm{d}\eta$. This is due to the different relative production suppression between $^3\overline{\text{He}}$ and $\bar{\text{t}}$ from their own sizes at different hadronic system scales.

4 Results of hypertriton and Ω-hypernuclei

This section presents the use of the coalescence model presented in Sect. 2 to study the production of the hypertriton $^3_\Lambda$H and Ω-hypernuclei. Results of the p_T spectra, the averaged p_T, and the yield rapidity densities of $^3_\Lambda$H are presented. Predictions of different Ω-hypernuclei, $H(\mathrm{p}\Omega^-)$, $H(\mathrm{n}\Omega^-)$, and $H(\mathrm{pn}\Omega^-)$ are reported. We propose two groups of observables, both of which exhibit novel behaviors. One group refers to the averaged transverse momentum ratios of light nuclei to the proton and hypernuclei to hyperons. The other is the centrality-dependent yield ratios of light (hyper-) nuclei to the protons (hyperons).

4.1 p_T spectra of Λ and Ω^- hyperons

The p_T spectra of Λ and Ω^- hyperons are necessary for computing p_T distributions of $^3_\Lambda$H and Ω-hypernuclei. We use the blast-wave model to get p_T distribution functions by fitting the experimental data of Λ and Ω^- in Pb+Pb collisions at $\sqrt{s_{\mathrm{NN}}} = 5.02$ TeV in 0–10%, 10–30%, and 30–50% centralities [84]. They are shown in Fig. 9. Filled symbols with error bars represent experimental data [84], and dashed lines represent the results of the blast-wave model. Values of the blast-wave fit parameters for Λ and Ω^- are listed in Table 2. The p_T spectra in 0–10%, 10–30%, and 30-50% centralities are scaled by 2^0, 2^{-1}, and 2^{-2}, respectively, for clarity in the figure. We have also studied the p_T spectra of Λ and Ω^- hyperons with the Quark Combination Model developed by the Shandong group (SDQCM) in another work [85], where the results are consistent with the blast-wave model results at low and intermediate p_T regions. Thus, we adopted these Λ and Ω^- hyperons in Fig. 9 to compute productions of the $^3_\Lambda$H and Ω-hypernuclei. The values of parameters a and b in $R_f(p_T)$ for $H(\mathrm{p}\Omega^-)$ and $H(\mathrm{n}\Omega^-)$ are the same as those for the deuteron, and those for $^3_\Lambda$H and $H(\mathrm{pn}\Omega^-)$ are the same as the values for ^{3}He. Thus, our calculated results for the $^3_\Lambda$H and Ω-hypernuclei are parameter-free, and they are more potent for further testing of the coalescence mechanism in describing the production of nuclei with strangeness flavor quantum number.

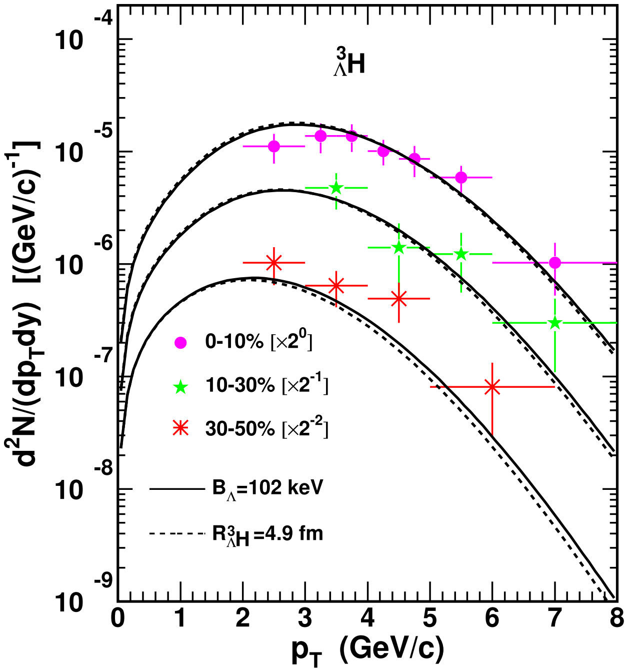

Fig. 10 (Color online) p_T spectra of the $^3_\Lambda$H in different centralities in Pb+Pb collisions at $\sqrt{s_{\mathrm{NN}}} = 5.02$ TeV. Filled symbols with error bars represent the experimental data [64]. The solid and dashed lines represent the theoretical results with a halo structure and a spherical shape, respectively

4.2 Results of the $^3_\Lambda$H

Based on Eq. (27), we compute the production of the $^3_\Lambda$H. Considering that the experimental measurements of the $^3_\Lambda$H suggest a halo structure with a d core encircled by a Λ, we first use $\sigma_1 = \sqrt{\frac{2(m_\mathrm{p}+m_\mathrm{n})^2}{3(m_\mathrm{p}^2+m_\mathrm{n}^2)}} R_\mathrm{d}$ and $\sigma_2 = \sqrt{\frac{2(m_\mathrm{d}+m_\Lambda)^2}{9(m_\mathrm{d}^2+m_\Lambda^2)}} r_{\Lambda\mathrm{d}}$. The $\Lambda-\mathrm{d}$ distance $r_{\Lambda\mathrm{d}}$ is evaluated via $r_{\Lambda\mathrm{d}} = \sqrt{\hbar^2/(4\mu B_\Lambda)}$ [86], where μ is the reduced mass, and the binding energy B_Λ is adopted to be the latest and most precise measurement reported to date 102 keV [63]. We also considered a spherical shape for the $^3_\Lambda$H to execute the calculation to evaluate the influence of the shape on its production. In this case, $\sigma_1 = \sqrt{\frac{m_\Lambda(m_\mathrm{p}+m_\mathrm{n})(m_\mathrm{p}+m_\mathrm{n}+m_\Lambda)}{m_\mathrm{p}m_\mathrm{n}(m_\mathrm{p}+m_\mathrm{n})+m_\mathrm{n}m_\Lambda(m_\mathrm{n}+m_\Lambda)+m_\Lambda m_\mathrm{p}(m_\Lambda+m_\mathrm{p})}} R_{^3_\Lambda\mathrm{H}}$, $\sigma_2 = \sqrt{\frac{4m_\mathrm{p}m_\mathrm{n}(m_\mathrm{p}+m_\mathrm{n}+m_\Lambda)^2}{3(m_\mathrm{p}+m_\mathrm{n})[m_\mathrm{p}m_\mathrm{n}(m_\mathrm{p}+m_\mathrm{n})+m_\mathrm{n}m_\Lambda(m_\mathrm{n}+m_\Lambda)+m_\Lambda m_\mathrm{p}(m_\Lambda+m_\mathrm{p})]}} R_{^3_\Lambda\mathrm{H}}$, where

Table 3 Averaged transverse momenta $\langle p_T \rangle$ and yield rapidity densities dN/dy of ${}^{3}_{\Lambda}$H in different centralities in Pb+Pb collisions at $\sqrt{s_{NN}} = 5.02$ TeV. Experimental data in the seventh column are obtained from Ref. [64]. Theory–4.9 denotes the theoretical results for the model with a spherical shape at $R_{{}^{3}_{\Lambda}\mathrm{H}} = 4.9$ fm. Theory-102, Theory-148, and Theory-410 denote the theoretical results for the model with a halo structure at B_Λ =102, 148, and 410 keV, respectively

	Centrality	$\langle p_T \rangle$ (GeV/c)				dN/dy $(\times 10^{-5})$				
		Theory–4.9	Theory-102	Theory-148	Theory-410	Data	Theory–4.9	Theory-102	Theory-148	Theory-410
${}^{3}_{\Lambda}$H	0–10%	3.16	3.19	3.24	3.37	$4.83 \pm 0.23 \pm 0.57$	6.09	5.96	7.75	12.7
	10–30%	2.90	2.94	2.99	3.11	$2.62 \pm 0.25 \pm 0.40$	2.98	2.99	4.07	7.44
	30–50%	2.46	2.52	2.55	2.65	$1.27 \pm 0.10 \pm 0.14$	0.875	0.932	1.35	2.94

the root-mean-square radius $R_{{}^{3}_{\Lambda}\mathrm{H}}$ is adopted to be 4.9 fm [2]. Figure 10 shows the p_T spectra of the ${}^{3}_{\Lambda}$H in 0–10%, 10–30%, and 30–50% centralities in Pb+Pb collisions at $\sqrt{s_{NN}} = 5.02$ TeV. Filled symbols with error bars represent the experimental data [64]. Solid lines represent the theoretical results of the coalescence model with the halo structure, and dashed lines represent the results for the model with the spherical shape. The p_T spectra in different centralities are scaled by different factors for clarity, as shown in the figure. As observed from Fig. 10, a weak difference exists in the theoretical results of the p_T spectra between the halo structure and the spherical shape, and the latter gives a little softer p_T spectra. The results with a halo structure approach the available data better, for amplitude and shape. This is also observed in the averaged transverse momenta $\langle p_T \rangle$ results and yield rapidity densities dN/dy of ${}^{3}_{\Lambda}$H.

Table 3 presents $\langle p_T \rangle$ and dN/dy of ${}^{3}_{\Lambda}$H in different centralities in Pb+Pb collisions at $\sqrt{s_{NN}} = 5.02$ TeV. Experimental data in the seventh column are obtained from Ref. [64]. Theory −4.9 in the third and eighth columns denotes the theoretical results for the model with a spherical shape at $R_{{}^{3}_{\Lambda}\mathrm{H}} = 4.9$ fm. Theory-102 in the fourth and ninth columns represents the theoretical results at $B_\Lambda = 102$ keV. Theory-148 in the fifth and tenth columns represents the theoretical results at a word averaged value of $B_\Lambda = 148$ keV [63]. We also present the theoretical results at $B_\Lambda = 410$ keV measured by the STAR collaboration [38] in the sixth and eleventh columns. Clear decreasing trends for $\langle p_T \rangle$ and dN/dy from central to semi-central collisions are observed. This is the same as the results for light nuclei; this is because, in more central collisions, more energy is deposited in the midrapidity region, and collective evolution exists for longer. For the halo structure, with the increase of the B_Λ, the size of the ${}^{3}_{\Lambda}$H decreases, and the suppression effect from the ${}^{3}_{\Lambda}$H size becomes relatively weak. This leads to an increase of dN/dy with the increasing B_Λ. Besides dN/dy, such production suppression effect also affects the p_T distribution [61, 87]. This is because the suppression effect becomes stronger with a larger nucleus size in a smaller system. Recalling that $R_f(p_T)$ decreases with p_T, the ${}^{3}_{\Lambda}$H production is more suppressed in larger p_T areas in the case of larger ${}^{3}_{\Lambda}$H size. Hence, $\langle p_T \rangle$ follows a decreasing trend with the decreasing B_Λ, as listed in Table 3. This is why the $\langle p_T \rangle$ of ${}^{3}_{\Lambda}$H is even smaller than that of the triton, whereas the $\langle p_T \rangle$ of Λ is larger than that of the nucleon.

Owing to its small binding energy compared to other light (hyper-)nuclei, the ${}^{3}_{\Lambda}$H has a very loosely-bound structure and a relatively large size. It would be easily destroyed after its formation from freeze-out nucleons and Λ's. As a result, the ${}^{3}_{\Lambda}$H is more likely to be produced later than the kinetic freeze-out time for the hadronic matter. In Ref. [88], the dependence of the yield of the ${}^{3}_{\Lambda}$H on its freeze-out time has

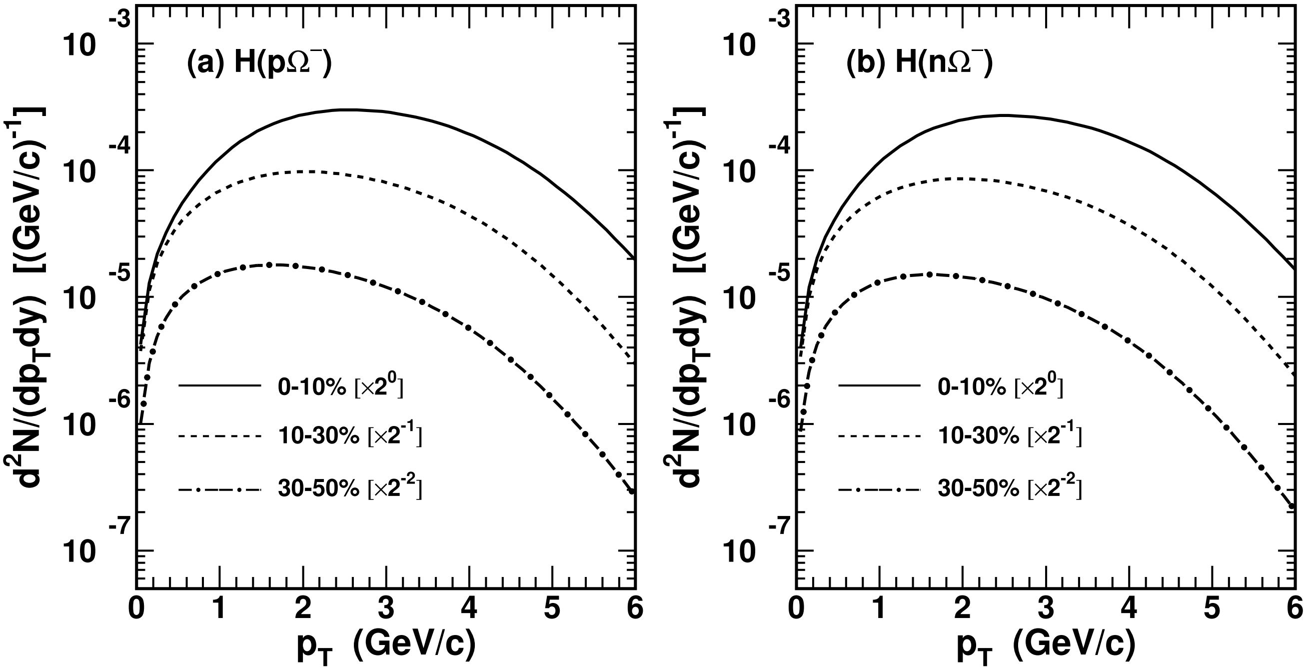

Fig. 11 Predictions of the p_T spectra of (**a**) $H(p\Omega^-)$ and (**b**) $H(n\Omega^-)$ in different centralities in Pb+Pb collisions at $\sqrt{s_{NN}} = 5.02$ TeV

Table 4 Predictions of averaged transverse momenta $\langle p_T \rangle$ and yield rapidity densities dN/dy of $H(p\Omega^-)$ and $H(n\Omega^-)$ in different centralities in Pb+Pb collisions at $\sqrt{s_{NN}} = 5.02$ TeV

	Centrality	$\langle p_T \rangle$ (GeV/c)	dN/dy ($\times 10^{-4}$)
$H(p\Omega^-)$	0–10%	2.84	9.80
	10–30%	2.44	6.27
	30–50%	2.18	2.16
$H(n\Omega^-)$	0–10%	2.81	8.75
	10–30%	2.41	5.46
	30–50%	2.15	1.79

been studied, and found that the dependence is very weak. This suggests that $^{3}_{\Lambda}$H abundance is essentially determined when nucleons and Λ's freeze-out from the system. So our coalescence calculations based on the same kinetic freeze-out with light nuclei can still reasonably describe the experimental data of $^{3}_{\Lambda}$H.

4.3 Predictions of Ω-hypernuclei

The nucleon-Ω dibaryon in the S-wave and spin-2 channel is an interesting candidate for the deuteron-like state [89, 90]. The HAL QCD collaboration has reported the root-mean-square radius of $H(p\Omega^-)$ is about 3.24 fm and that of $H(n\Omega^-)$ is 3.77 fm [91]. According to Eq. (15), we study their productions, where the spin degeneracy factor $g_{H(p\Omega^-)} = g_{H(n\Omega^-)} = 5/8$. Fig. 11 shows predictions for their p_T spectra in $0-10\%$, $10-30\%$, and $30-50\%$ centralities with solid, dashed, and dash-dotted lines, respectively, in Pb+Pb collisions at $\sqrt{s_{NN}} = 5.02$ TeV. Different lines are scaled by different factors for clarity, as shown in figure.

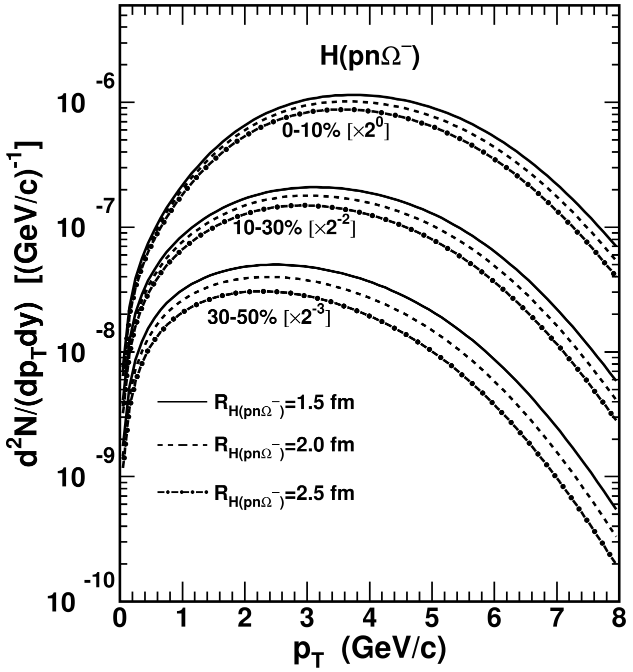

Fig. 12 Predictions of the p_T spectra of $H(pn\Omega^-)$ in different centralities in Pb+Pb collisions at $\sqrt{s_{NN}} = 5.02$ TeV

Table 5 Predictions of averaged transverse momenta $\langle p_T \rangle$ and yield rapidity densities dN/dy of $H(pn\Omega^-)$ in different centralities in Pb+Pb collisions at $\sqrt{s_{NN}}$ = 5.02 TeV. Theory−1.5, Theory−2.0, and Theory−2.5 denote the theoretical results at $R_{H(pn\Omega^-)}$ =1.5, 2.0, and 2.5 fm, respectively

	Centrality	$\langle p_T \rangle$ (GeV/c)			dN/dy ($\times 10^{-6}$)		
		Theory−1.5	Theory−2.0	Theory−2.5	Theory−1.5	Theory−2.0	Theory−2.5
$H(pn\Omega^-)$	0–10%	3.94	3.88	3.82	4.77	4.17	3.56
	10–30%	3.44	3.36	3.29	3.50	2.95	2.41
	30–50%	2.98	2.89	2.81	1.60	1.24	0.92

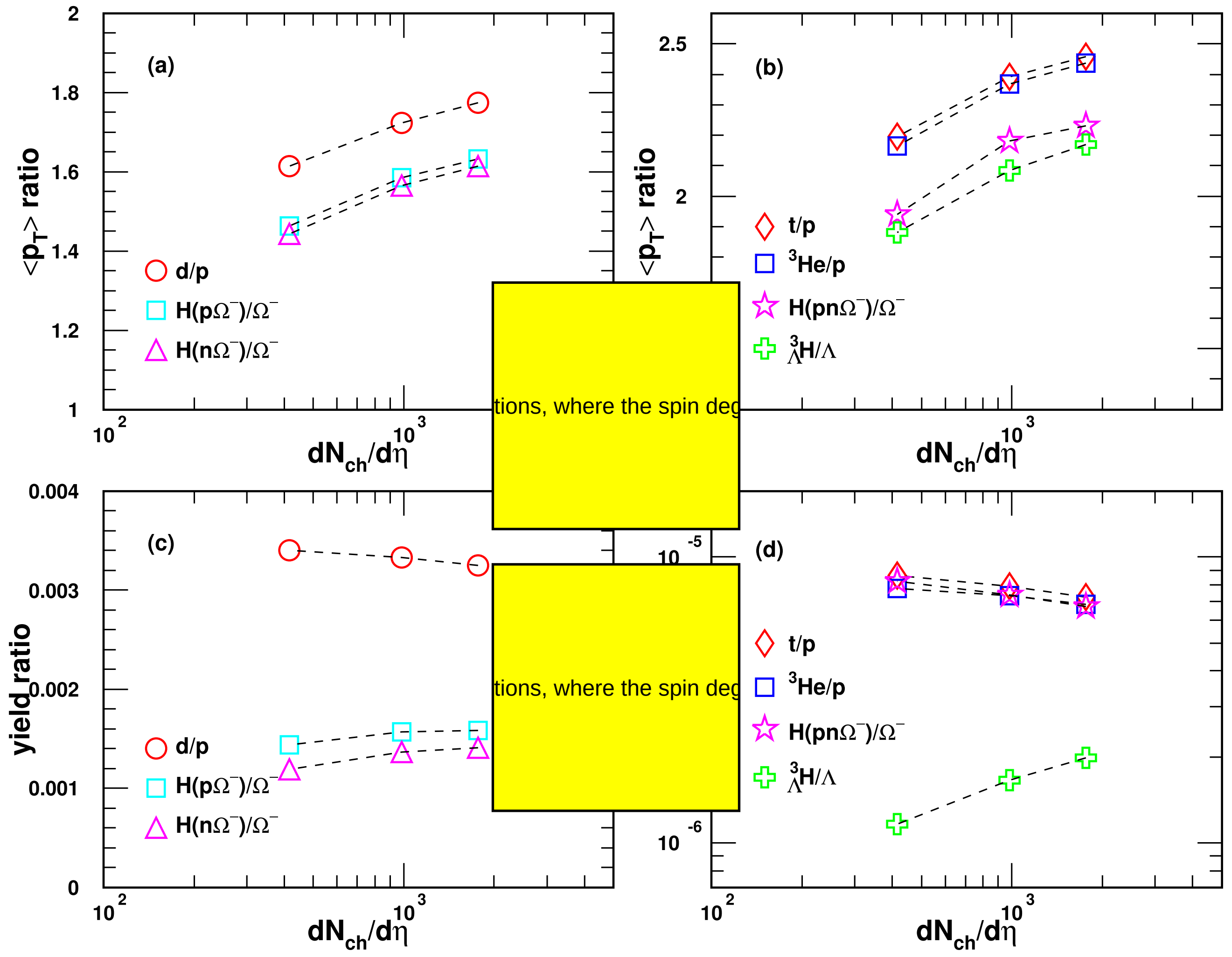

Fig. 13 The $\langle p_T \rangle$ ratios of (**a**) dibaryon states to baryons, (**b**) tribaryon states to baryons, and the yield ratios of (**c**) dibaryon states to baryons, and (**d**) tribaryon states to baryons as a function of $dN_{ch}/d\eta$ in Pb+Pb collisions at $\sqrt{s_{NN}}$ = 5.02 TeV. Different open symbols connected with dashed lines to guide the eye are the theoretical results

Table 4 presents predictions of the averaged transverse momenta $\langle p_T \rangle$ and yield rapidity densities dN/dy of $H(p\Omega^-)$ and $H(n\Omega^-)$. Both of them decrease from central to semi-central collisions, similar to light nuclei and the ${}^3_\Lambda$H. The slightly lower results of $H(n\Omega^-)$ than $H(p\Omega^-)$ come from its slightly larger size.

The $H(pn\Omega^-)$ with maximal spin-$\frac{5}{2}$ is proposed to be one of the most promising partners of the t and ${}^3_\Lambda$H with multi-strangeness flavor quantum number [92]. With Eq. (27), we study its production and the spin degeneracy factor $g_{H(pn\Omega^-)} = 3/8$. As its root-mean-square radius $R_{H(pn\Omega^-)}$ is undetermined, we adopt 1.5, 2.0, and 2.5 fm to execute calculations, respectively. Figure 12 shows predictions of the p_{T} spectra in 0–10%, 10–30% and 30–50% centralities in Pb+Pb collisions at $\sqrt{s_{\mathrm{NN}}} = 5.02$ TeV. Solid, dashed, and dash-dotted lines denote results with $R_{H(\mathrm{pn}\Omega^-)}$ =1.5, 2.0, and 2.5 fm, respectively, which are scaled by different factors for clarity as shown in the figure. Table 5 presents predictions of the averaged transverse momenta $\langle p_{\mathrm{T}} \rangle$ and yield rapidity densities $\mathrm{d}N/\mathrm{d}y$ of $H(\mathrm{pn}\Omega^-)$. Theory−1.5, Theory−2.0, and Theory−2.5 denote the theoretical results at $R_{H(\mathrm{pn}\Omega^-)}$ =1.5, 2.0, and 2.5 fm, respectively.

Our predictions in the central collisions for $H(\mathrm{p}\Omega^-)$ and $H(\mathrm{n}\Omega^-)$ are of the same magnitude as those with BLWC and AMPTC models in Ref. [93], and those for $H(\mathrm{pn}\Omega^-)$ are of the same magnitude as reported in Ref. [94]. Our predictions in other centralities provide more detailed references for centrality-dependent measurements of these Ω-hypernuclei in future LHC experiments.

4.4 Averaged transverse momentum ratios and yield ratios

Based on the results of light nuclei and hypernuclei presented above, we study two groups of interesting observables as powerful probes for the production correlations of different species of nuclei. One group refers to the $\langle p_{\mathrm{T}} \rangle$ ratios of light nuclei to the proton and hypernuclei to hyperons. The other is their centrality-dependent yield ratios.

Figure 13(a) and (b) show the $\langle p_{\mathrm{T}} \rangle$ ratios of dibaryon states to baryons and those of tribaryon states to baryons, i.e., $\frac{\langle p_{\mathrm{T}} \rangle_{\mathrm{d}}}{\langle p_{\mathrm{T}} \rangle_{\mathrm{p}}}$, $\frac{\langle p_{\mathrm{T}} \rangle_{H(\mathrm{p}\Omega^-)}}{\langle p_{\mathrm{T}} \rangle_{\Omega^-}}$, $\frac{\langle p_{\mathrm{T}} \rangle_{H(\mathrm{n}\Omega^-)}}{\langle p_{\mathrm{T}} \rangle_{\Omega^-}}$, $\frac{\langle p_{\mathrm{T}} \rangle_{\mathrm{t}}}{\langle p_{T} \rangle_{\mathrm{p}}}$, $\frac{\langle p_{\mathrm{T}} \rangle_{^3\mathrm{He}}}{\langle p_{\mathrm{T}} \rangle_{\mathrm{p}}}$, $\frac{\langle p_{\mathrm{T}} \rangle_{^3_\Lambda\mathrm{H}}}{\langle p_{\mathrm{T}} \rangle_{\Lambda}}$ and $\frac{\langle p_{\mathrm{T}} \rangle_{H(\mathrm{pn}\Omega^-)}}{\langle p_{\mathrm{T}} \rangle_{\Omega^-}}$. Open symbols connected by dashed lines to guide the eye represent the theoretical results of the coalescence model. All these $\langle p_{\mathrm{T}} \rangle$ ratios increase as a function of $\mathrm{d}N_{\mathrm{ch}}/\mathrm{d}\eta$ owing to the stronger collective flow in more central collisions. More interestingly, these $\langle p_{\mathrm{T}} \rangle$ ratios of light nuclei to nucleons and hypernuclei to hyperons happen to offset the $\langle p_{\mathrm{T}} \rangle$ differences of p, Λ, and Ω^-. This makes them more powerful in bringing the characteristics resulting from the production mechanism to light. Both dibaryon-to-baryon and tribaryon-to-baryon $\langle p_{\mathrm{T}} \rangle$ ratios exhibit a reverse hierarchy of the nucleus sizes at any centrality, i.e., $\frac{\langle p_{\mathrm{T}} \rangle_{\mathrm{d}}}{\langle p_{\mathrm{T}} \rangle_{\mathrm{p}}} > \frac{\langle p_{\mathrm{T}} \rangle_{H(\mathrm{p}\Omega^-)}}{\langle p_{\mathrm{T}} \rangle_{\Omega^-}} > \frac{\langle p_{\mathrm{T}} \rangle_{H(\mathrm{n}\Omega^-)}}{\langle p_{\mathrm{T}} \rangle_{\Omega^-}}$ as $R_{\mathrm{d}} < R_{H(\mathrm{p}\Omega^-)} < R_{H(\mathrm{n}\Omega^-)}$, and $\frac{\langle p_{\mathrm{T}} \rangle_{\mathrm{t}}}{\langle p_{\mathrm{T}} \rangle_{\mathrm{p}}} > \frac{\langle p_{\mathrm{T}} \rangle_{^3\mathrm{He}}}{\langle p_{\mathrm{T}} \rangle_{\mathrm{p}}} > \frac{\langle p_{\mathrm{T}} \rangle_{H(\mathrm{pn}\Omega^-)}}{\langle p_{\mathrm{T}} \rangle_{\Omega^-}} > \frac{\langle p_{\mathrm{T}} \rangle_{^3_\Lambda\mathrm{H}}}{\langle p_{\mathrm{T}} \rangle_{\Lambda}}$ as $R_{\mathrm{t}} < R_{^3\mathrm{He}} < R_{H(\mathrm{pn}\Omega^-)} < R_{^3_\Lambda\mathrm{H}}$. Here, we consider results of $H(\mathrm{pn}\Omega^-)$ at $R_{H(\mathrm{pn}\Omega^-)} = 2$ fm for exhibition, and those at $R_{H(\mathrm{pn}\Omega^-)} = 1.5, 2.5$ fm give the same conclusion, a reverse hierarchy of the nucleus size. Such reverse hierarchy comes from stronger production suppression for light (hyper-) nuclei with larger sizes in higher p_{T} regions. This production property is considerably different from the thermal model in which these ratios are approximately equal to each other [43].

Figure 13(c) and (d) show yield ratios of dibaryon states to baryons and those of tribaryon states to baryons. Open symbols connected with dashed lines to guide the eye represent the theoretical results of the coalescence model. Some of these ratios such as d/p, t/p, ^{3}He/p and $H(\mathrm{pn}\Omega^-)/\Omega^-$ decrease while the others $H(\mathrm{p}\Omega^-)/\Omega^-$, $H(\mathrm{n}\Omega^-)/\Omega^-$ and $^3_\Lambda\mathrm{H}/\Lambda$ increase as a function of $\mathrm{d}N_{\mathrm{ch}}/\mathrm{d}\eta$.

From Eqs. (15) and (27), similar as Eq. (34), we approximately have

$$\begin{aligned}
&\frac{\mathrm{d}}{\mathrm{p}} \sim \frac{H(\mathrm{p}\Omega^-)}{\Omega^-} \sim \frac{H(\mathrm{n}\Omega^-)}{\Omega^-} \\
&\propto \frac{N_{\mathrm{p}}}{\langle R_{\mathrm{f}} \rangle^3 \left(C_0 + \frac{\sigma^2}{\langle R_{\mathrm{f}} \rangle^2} \right) \sqrt{\frac{C_0}{\langle \gamma \rangle^2} + \frac{\sigma^2}{\langle R_{\mathrm{f}} \rangle^2}}} \\
&= \frac{N_{\mathrm{p}}}{\langle R_{\mathrm{f}} \rangle^3 / \langle \gamma \rangle} \times \frac{1}{\left(C_0 + \frac{\sigma^2}{\langle R_f \rangle^2} \right) \sqrt{C_0 + \frac{\sigma^2}{\langle R_{\mathrm{f}} \rangle^2 / \langle \gamma \rangle^2}}},
\end{aligned} \tag{35}$$

and

$$\begin{aligned}
&\frac{\mathrm{t}}{\mathrm{p}} \sim \frac{^3\mathrm{He}}{\mathrm{p}} \sim \frac{^3_\Lambda\mathrm{H}}{\Lambda} \sim \frac{H(\mathrm{pn}\Omega^-)}{\Omega^-} \\
&\propto \frac{N_{\mathrm{p}}^2}{\langle R_{\mathrm{f}} \rangle^6 \left(C_0 + \frac{\sigma_1^2}{\langle R_{\mathrm{f}} \rangle^2} \right) \sqrt{\frac{C_0}{\langle \gamma \rangle^2} + \frac{\sigma_1^2}{\langle R_{\mathrm{f}} \rangle^2}}} \\
&\quad \times \frac{1}{\left(\frac{4C_0}{3} + \frac{\sigma_2^2}{\langle R_{\mathrm{f}} \rangle^2} \right) \sqrt{\frac{4C_0}{3\langle \gamma \rangle^2} + \frac{\sigma_2^2}{\langle R_{\mathrm{f}} \rangle^2}}} \\
&= \left(\frac{N_{\mathrm{p}}}{\langle R_{\mathrm{f}} \rangle^3 / \langle \gamma \rangle} \right)^2 \frac{1}{\left(C_0 + \frac{\sigma_1^2}{\langle R_{\mathrm{f}} \rangle^2} \right) \sqrt{C_0 + \frac{\sigma_1^2}{\langle R_{\mathrm{f}} \rangle^2 / \langle \gamma \rangle^2}}} \\
&\quad \times \frac{1}{\left(\frac{4C_0}{3} + \frac{\sigma_2^2}{\langle R_{\mathrm{f}} \rangle^2} \right) \sqrt{\frac{4C_0}{3} + \frac{\sigma_2^2}{\langle R_{\mathrm{f}} \rangle^2 / \langle \gamma \rangle^2}}}.
\end{aligned} \tag{36}$$

Eqs. (35) and (36) show that behaviors of these two-particle yield ratios closely relate with the nucleon number density $\frac{N_{\mathrm{p}}}{\langle R_{\mathrm{f}} \rangle^3 / \langle \gamma \rangle}$ and the production suppression effect items of the relative size of nuclei to hadronic source systems $\frac{\sigma}{\langle R_{\mathrm{f}} \rangle}$, $\frac{\sigma_1}{\langle R_{\mathrm{f}} \rangle}$ and $\frac{\sigma_2}{\langle R_{\mathrm{f}} \rangle}$.

For the limit case of the nuclei with considerably small (negligible) sizes compared to the hadronic system scale, the $\mathrm{d}N_{\mathrm{ch}}/\mathrm{d}\eta$-dependent behaviors of their yield ratios to baryons are completely determined by the nucleon number density. For the general case, the item $\frac{\sigma_i}{\langle R_{\mathrm{f}} \rangle}$ suppresses these ratios, and such suppression becomes weaker in larger hadronic systems. This makes these yield ratios increase from peripheral to central collisions, i.e., with the increasing $\mathrm{d}N_{\mathrm{ch}}/\mathrm{d}\eta$. The larger the nucleus size, the stronger the increase as a function of $\mathrm{d}N_{\mathrm{ch}}/\mathrm{d}\eta$. The nucleon density decreases with increasing $\mathrm{d}N_{\mathrm{ch}}/\mathrm{d}\eta$ [80], which makes these ratios decrease. As the root-mean-square radii of d, t, ${}^{3}\mathrm{He}$, and $H(\mathrm{pn}\Omega^{-})$ are approximately equal or smaller than 2 fm, the decreasing nucleon density dominates the behaviors of their yield ratios to baryons. But for $H(\mathrm{p}\Omega^{-})$, $H(\mathrm{n}\Omega^{-})$ and ${}^{3}_{\Lambda}\mathrm{H}$, their root-mean-square radii are larger than 3 fm, the production suppression effect from their sizes becomes dominant, which leads their yield ratios to baryons increase as a function of $\mathrm{d}N_{\mathrm{ch}}/\mathrm{d}\eta$. Such different centrality-dependent behaviors can help justify the sizes of more light nuclei and hypernuclei in future experiments.

5 Summary

This study extended the analytical coalescence model previously developed for the productions of light nuclei to include the hyperon coalescence to simultaneously study the production characteristics of d, ${}^{3}\overline{\mathrm{He}}$, $\bar{\mathrm{t}}$, ${}^{3}_{\Lambda}\mathrm{H}$, and Ω-hypernuclei. To this end, the formulae of momentum distributions of two baryons coalescing into dibaryon states and three baryons coalescing into tribaryon states were derived. The relationships of dibaryon states and tribaryon states with primordial baryons in momentum space in the laboratory frame were presented, and the effects of the hadronic system scale and the nucleus's size on the nucleus production were demonstrated.

The extended coalescence model was applied to Pb+Pb collisions at $\sqrt{s_{\mathrm{NN}}} = 5.02\,\mathrm{TeV}$. Available data on B_2 and B_3, p_{T} spectra, averaged transverse momenta, and yield rapidity densities of the d, ${}^{3}\overline{\mathrm{He}}$, $\bar{\mathrm{t}}$, and ${}^{3}_{\Lambda}\mathrm{H}$ measured by the ALICE collaboration were explained. Moreover, the p_{T} spectra, averaged transverse momenta, and yield rapidity densities of different Ω-hypernuclei, e.g., $H(\mathrm{p}\Omega^{-})$, $H(\mathrm{n}\Omega^{-})$, and $H(\mathrm{pn}\Omega^{-})$, were predicted for future experimental measurements.

Notably, this study presented two groups of novel observables. One referred to the averaged transverse momentum ratios $\frac{\langle p_{\mathrm{T}}\rangle_{\mathrm{d}}}{\langle p_{\mathrm{T}}\rangle_{\mathrm{p}}}$, $\frac{\langle p_{\mathrm{T}}\rangle_{H(\mathrm{p}\Omega^{-})}}{\langle p_{\mathrm{T}}\rangle_{\Omega^{-}}}$, $\frac{\langle p_{\mathrm{T}}\rangle_{H(\mathrm{n}\Omega^{-})}}{\langle p_{\mathrm{T}}\rangle_{\Omega^{-}}}$, $\frac{\langle p_{\mathrm{T}}\rangle_{\mathrm{t}}}{\langle p_{\mathrm{T}}\rangle_{\mathrm{p}}}$, $\frac{\langle p_{\mathrm{T}}\rangle_{{}^{3}\mathrm{He}}}{\langle p_{\mathrm{T}}\rangle_{\mathrm{p}}}$, $\frac{\langle p_{\mathrm{T}}\rangle_{{}^{3}_{\Lambda}\mathrm{H}}}{\langle p_{\mathrm{T}}\rangle_{\Lambda}}$, and $\frac{\langle p_{\mathrm{T}}\rangle_{H(\mathrm{pn}\Omega^{-})}}{\langle p_{\mathrm{T}}\rangle_{\Omega^{-}}}$. These ratios exhibited a reverse hierarchy according to the sizes of the nuclei themselves at any collision centrality. The other group of observables involved the centrality-dependent yield ratios $\frac{\mathrm{d}}{\mathrm{p}}$, $\frac{H(\mathrm{p}\Omega^{-})}{\Omega^{-}}$, $\frac{H(\mathrm{n}\Omega^{-})}{\Omega^{-}}$, $\frac{\mathrm{t}}{\mathrm{p}}$, $\frac{{}^{3}\mathrm{He}}{\mathrm{p}}$, $\frac{{}^{3}_{\Lambda}\mathrm{H}}{\Lambda}$, and $\frac{H(\mathrm{pn}\Omega^{-})}{\Omega^{-}}$. Some of these yield ratios $\frac{\mathrm{d}}{\mathrm{p}}$, $\frac{\mathrm{t}}{\mathrm{p}}$, $\frac{{}^{3}\mathrm{He}}{\mathrm{p}}$, and $\frac{H(\mathrm{pn}\Omega^{-})}{\Omega^{-}}$ decreased while the others $\frac{H(\mathrm{p}\Omega^{-})}{\Omega^{-}}$, $\frac{H(\mathrm{n}\Omega^{-})}{\Omega^{-}}$, and $\frac{{}^{3}_{\Lambda}\mathrm{H}}{\Lambda}$ increased as a function of $\mathrm{d}N_{\mathrm{ch}}/\mathrm{d}\eta$. Such different trends were caused by different production suppression degrees from the nucleus sizes. The behaviors of these two groups of ratios in the coalescence mechanism were different from the thermal model. Therefore, these are powerful observables for probing the production mechanism of light (hyper-)nuclei and can reveal the production mechanisms of different types of nuclei in the coalescence framework.

Author contributions All authors contributed to the study conception and design. Material preparation, data collection and analysis were performed by Rui-Qin Wang, Xin-Lei Hou, Yan-Hao Li, Jun Song, and Feng-Lan Shao. The first draft of the manuscript was written by Rui-Qin Wang and all authors commented on previous versions of the manuscript. All authors read and approved the final manuscript.

Declarations

Conflict of interest The authors declare that they have no conflict of interest.

References

1. J. Chen, D. Keane, Y.G. Ma et al., Antinuclei in heavy-ion collisions. Phys. Rept. **760**, 1–39 (2018). https://doi.org/10.1016/j.physrep.2018.07.002. arXiv:1808.09619
2. H. Nemura, Y. Suzuki, Y. Fujiwara et al., Study of light Lambda and Lambda-Lambda hypernuclei with the stochastic variational method and effective Lambda N potentials. Prog. Theor. Phys. **103**, 929–958 (2000). https://doi.org/10.1143/PTP.103.929
3. D. Oliinychenko, Overview of light nuclei production in relativistic heavy-ion collisions. Nucl. Phys. A **1005**, 121754 (2021). https://doi.org/10.1016/j.nuclphysa.2020.121754. arXiv:2003.05476
4. K.J. Sun, L.W. Chen, C.M. Ko et al., Light nuclei production as a probe of the QCD phase diagram. Phys. Lett. B **781**, 499–504 (2018). https://doi.org/10.1016/j.physletb.2018.04.035. arXiv:1801.09382
5. K. Blum, M. Takimoto, Nuclear coalescence from correlation functions. Phys. Rev. C **99**, 044913 (2019). https://doi.org/10.1103/PhysRevC.99.044913. arXiv:1901.07088
6. P. Braun-Munzinger, B. Dönigus, Loosely-bound objects produced in nuclear collisions at the LHC. Nucl. Phys. A **987**, 144–201 (2019). https://doi.org/10.1016/j.nuclphysa.2019.02.006. arXiv:1809.04681
7. S. Mrowczynski, Production of light nuclei at colliders–coalescence vs thermal model. Eur. Phys. J. ST **229**, 3559–3583 (2020). https://doi.org/10.1140/epjst/e2020-000067-0
8. R. Wang, Y.G. Ma, L.W. Chen et al., Kinetic approach of light-nuclei production in intermediate-energy heavy-ion collisions. Phys. Rev. C **108**, L031601 (2023). https://doi.org/10.1103/PhysRevC.108.L031601. arXiv:2305.02988
9. J. Aichelin, "Quantum'' molecular dynamics: a dynamical microscopic n body approach to investigate fragment formation and the nuclear equation of state in heavy ion collisions. Phys. Rept. **202**, 233–360 (1991). https://doi.org/10.1016/0370-1573(91)90094-3
10. K.J. Sun, R. Wang, C.M. Ko et al., Unveiling the dynamics of little-bang nucleosynthesis. Nature Commun. **15**, 1074 (2024). https://doi.org/10.1038/s41467-024-45474-x. arXiv:2207.12532
11. A. Andronic, P. Braun-Munzinger, K. Redlich et al., Decoding the phase structure of QCD via particle production at high

energy. Nature **561**, 321–330 (2018). https://doi.org/10.1038/s41586-018-0491-6. arXiv:1710.09425

12. K.J. Sun, L.W. Chen, C.M. Ko et al., Probing QCD critical fluctuations from light nuclei production in relativistic heavy-ion collisions. Phys. Lett. B **774**, 103–107 (2017). https://doi.org/10.1016/j.physletb.2017.09.056. arXiv:1702.07620
13. A. Bzdak, S. Esumi, V. Koch et al., Mapping the phases of quantum chromodynamics with beam energy scan. Phys. Rept. **853**, 1–87 (2020). https://doi.org/10.1016/j.physrep.2020.01.005. arXiv:1906.00936
14. H. Liu, D. Zhang, S. He et al., Light nuclei production in Au+Au collisions at $\sqrt{s_{\mathrm{NN}}}$ = 5–200 GeV from JAM model. Phys. Lett. B **805**, 135452 (2020). https://doi.org/10.1016/j.physletb.2020.135452
15. X. Luo, S. Shi, N. Xu et al., A study of the properties of the QCD phase diagram in high-energy nuclear collisions. Particles **3**, 278–307 (2020). https://doi.org/10.3390/particles3020022. arXiv:2004.00789
16. J. Steinheimer, M. Mitrovski, T. Schuster et al., Strangeness fluctuations and MEMO production at FAIR. Phys. Lett. B **676**, 126–131 (2009). https://doi.org/10.1016/j.physletb.2009.04.062. arXiv:0811.4077
17. T. Shao, J. Chen, C.M. Ko et al., Yield ratio of hypertriton to light nuclei in heavy-ion collisions from $\sqrt{s_{\mathrm{NN}}}$ = 4.9 GeV to 2.76 TeV. Chin. Phys. C **44**, 114001 (2020). https://iopscience.iop.org/article/10.1088/1674-1137/abadf0
18. J.L. Nagle, B.S. Kumar, M.J. Bennett et al., Source size determination in relativistic nucleus-nucleus collisions. Phys. Rev. Lett. **73**, 1219–1222 (1994). https://doi.org/10.1103/PhysRevLett.73.1219
19. S. Bazak, S. Mrowczynski, Production of ^{4}Li and p$-^3$He correlation function in relativistic heavy-ion collisions. Eur. Phys. J. A **56**, 193 (2020). https://doi.org/10.1140/epja/s10050-020-00198-6
20. Y.X. Zhang, S. Zhang, Y.G. Ma, Deuteron production mechanism via azimuthal correlation for p − p and p-Pb collisions at LHC energy with the AMPT model. Eur. Phys. J. A **59**, 72 (2023). https://doi.org/10.1140/epja/s10050-023-00980-2
21. S.R. Beane, E. Chang, S.D. Cohen et al., Light nuclei and hypernuclei from quantum chromodynamics in the limit of SU(3) flavor symmetry. Phys. Rev. D **87**, 034506 (2013). https://doi.org/10.1103/PhysRevD.87.034506. arXiv:1206.5219
22. Y.G. Ma, Hypernuclei as a laboratory to test hyperon-nucleon interactions. Nucl. Sci. Tech. **34**, 97 (2023). https://doi.org/10.1007/s41365-023-01248-6
23. P. Junnarkar, N. Mathur, Deuteronlike heavy dibaryons from lattice quantum chromodynamics. Phys. Rev. Lett. **123**, 162003 (2019). https://doi.org/10.1103/PhysRevLett.123.162003. arXiv:1906.06054
24. K. Morita, S. Gongyo, T. Hatsuda et al., Probing ΩΩ and pΩ dibaryons with femtoscopic correlations in relativistic heavy-ion collisions. Phys. Rev. C **101**, 015201 (2020). https://doi.org/10.1103/PhysRevC.101.015201. arXiv:1908.05414
25. S. Afanasiev et al., Elliptic flow for phi mesons and (anti) deuterons in Au + Au collisions at $\sqrt{s_{\mathrm{NN}}}$ = 200-GeV. Phys. Rev. Lett. **99**, 052301 (2007). https://doi.org/10.1103/PhysRevLett.99.052301
26. T. Anticic et al., Production of deuterium, tritium, and ^{3}He in central Pb + Pb collisions at 20A, 30A, 40A, 80A, and 158A GeV at the CERN super proton synchrotron. Phys. Rev. C **94**, 044906 (2016). https://doi.org/10.1103/PhysRevC.94.044906. arXiv:1606.04234
27. C. Adler et al., Anti-deuteron and anti-He-3 production in $\sqrt{s_{\mathrm{NN}}}$ = 130-GeV Au+Au collisions. Phys. Rev. Lett. **87**, 262301 (2001). https://doi.org/10.1103/PhysRevLett.87.26230
28. J. Chen et al., Properties of the QCD matter: review of selected results from the relativistic heavy ion collider beam energy scan (RHIC BES) program. Nucl. Sci. Tech. **35**, 214 (2024). https://doi.org/10.1007/s41365-024-01591-2. arXiv:2407.02935
29. B. Dönigus, G. Röpke, D. Blaschke, Deuteron yields from heavy-ion collisions at energies available at the CERN large hadron collider: continuum correlations and in-medium effects. Phys. Rev. C **106**, 044908 (2022). https://doi.org/10.1103/PhysRevC.106.044908. arXiv:2206.10376
30. L.L. Zhu, B. Wang, M. Wang et al., Energy and centrality dependence of light nuclei production in relativistic heavy-ion collisions. Nucl. Sci. Tech. **33**, 45 (2022). https://doi.org/10.1007/s41365-022-01028-8
31. K.J. Sun, C.M. Ko, Event-by-event antideuteron multiplicity fluctuation in Pb+Pb collisions at $\sqrt{s_{\mathrm{NN}}}$ =5.02 TeV. Phys. Lett. B **840**, 137864 (2023). https://doi.org/10.1016/j.physletb.2023.137864
32. F. Li, S. Zhang, K.J. Sun et al., Production of light nuclei in isobaric Ru + Ru and Zr + Zr collisions at $\sqrt{s_{\mathrm{NN}}}$ =7.7–200 GeV from a multiphase transport model. Phys. Rev. C **109**, 064912 (2024). https://doi.org/10.1103/PhysRevC.109.064912
33. S. Acharya et al., Elliptic and triangular flow of (anti)deuterons in Pb–Pb collisions at $\sqrt{s_{\mathrm{NN}}}$ = 5.02 TeV. Phys. Rev. C **102**, 055203 (2020). https://doi.org/10.1103/PhysRevC.102.055203
34. L. Adamczyk et al., Measurement of elliptic flow of light nuclei at $\sqrt{s_{\mathrm{NN}}}$ = 200, 62.4, 39, 27, 19.6, 11.5, and 7.7 GeV at the BNL relativistic heavy ion collider. Phys. Rev. C **94**, 034908 (2016). https://doi.org/10.1103/PhysRevC.94.034908
35. J. Adam et al., Beam-energy dependence of the directed flow of deuterons in Au+Au collisions. Phys. Rev. C **102**, 044906 (2020). https://doi.org/10.1103/PhysRevC.102.044906. arXiv:2007.04609
36. J. Adam et al., Beam energy dependence of (anti-)deuteron production in Au + Au collisions at the BNL relativistic heavy ion collider. Phys. Rev. C **99**, 064905 (2019). https://doi.org/10.1103/PhysRevC.99.064905. arXiv:1903.11778
37. M. Abdulhamid et al., Beam energy dependence of triton production and yield ratio ($\mathrm{N_t \times N_p / N_d^2}$) in Au+Au collisions at RHIC. Phys. Rev. Lett. **130**, 202301 (2023). https://doi.org/10.1103/PhysRevLett.130.202301. arXiv:2209.08058
38. J. Adam et al., Measurement of the mass difference and the binding energy of the hypertriton and antihypertriton. Nat. Phys. **16**, 409–412 (2020). https://doi.org/10.1038/s41567-020-0799-7. arXiv:1904.10520
39. M. Abdallah et al., Measurements of H^3_Λ and H^4_Λ lifetimes and yields in Au+Au collisions in the high baryon density region. Phys. Rev. Lett. **128**, 202301 (2022). https://doi.org/10.1103/PhysRevLett.128.202301. arXiv:2110.09513
40. J. Adam et al., ${}^3_\Lambda\mathrm{H}$ and ${}^3_{\bar\Lambda}\bar{\mathrm{H}}$ production in Pb-Pb collisions at $\sqrt{s_{\mathrm{NN}}}$ = 2.76 TeV. Phys. Lett. B **754**, 360–372 (2016). https://doi.org/10.1016/j.physletb.2016.01.040
41. A. Mekjian, Thermodynamic model for composite particle emission in relativistic heavy ion collisions. Phys. Rev. Lett. **38**, 640–643 (1977). https://doi.org/10.1103/PhysRevLett.38.640
42. P.J. Siemens, J.I. Kapusta, Evidence for a soft nuclear matter equation of state. Phys. Rev. Lett. **43**, 1486–1489 (1979). https://doi.org/10.1103/PhysRevLett.43.1486
43. A. Andronic, P. Braun-Munzinger, J. Stachel et al., Production of light nuclei, hypernuclei and their antiparticles in relativistic nuclear collisions. Phys. Lett. B **697**, 203–207 (2011). https://doi.org/10.1016/j.physletb.2011.01.053. arXiv:1010.2995
44. J. Cleymans, S. Kabana, I. Kraus et al., Antimatter production in proton-proton and heavy-ion collisions at ultrarelativistic energies. Phys. Rev. C **84**, 054916 (2011). https://doi.org/10.1103/PhysRevC.84.054916. arXiv:1105.3719

45. Y. Cai, T.D. Cohen, B.A. Gelman et al., Yields of weakly-bound light nuclei as a probe of the statistical hadronization model. Phys. Rev. C **100**, 024911 (2019). https://doi.org/10.1103/PhysRevC.100.024911. arXiv:1905.02753
46. A. Schwarzschild, C. Zupancic, Production of tritons, deuterons, nucleons, and mesons by 30-GeV protons on A-1, Be, and Fe targets. Phys. Rev. **129**, 854–862 (1963). https://doi.org/10.1103/PhysRev.129.854
47. H. Sato, K. Yazaki, On the coalescence model for high-energy nuclear reactions. Phys. Lett. B **98**, 153–157 (1981). https://doi.org/10.1016/0370-2693(81)90976-X
48. R. Mattiello, A. Jahns, H. Sorge et al., Deuteron flow in ultrarelativistic heavy ion reactions. Phys. Rev. Lett. **74**, 2180–2183 (1995). https://doi.org/10.1103/PhysRevLett.74.2180
49. L.W. Chen, C.M. Ko, B.A. Li, Light clusters production as a probe to the nuclear symmetry energy. Phys. Rev. C **68**, 017601 (2003). https://doi.org/10.1103/PhysRevC.68.017601. arXiv:nucl-th/0302068
50. W. Zhao, L. Zhu, H. Zheng et al., Spectra and flow of light nuclei in relativistic heavy ion collisions at energies available at the BNL relativistic heavy ion collider and at the CERN large hadron collider. Phys. Rev. C **98**, 054905 (2018). https://doi.org/10.1103/PhysRevC.98.054905. arXiv:1807.02813
51. R. Mattiello, H. Sorge, H. Stocker et al., Nuclear clusters as a probe for expansion flow in heavy ion reactions at 10–15 A/GeV. Phys. Rev. C **55**, 1443–1454 (1997). https://doi.org/10.1103/PhysRevC.55.1443. arXiv:nucl-th/9607003
52. P. Liu, J.H. Chen, Y.G. Ma et al., Production of light nuclei and hypernuclei at High Intensity Accelerator Facility energy region. Nucl. Sci. Tech. **28**, 55 (2017). https://doi.org/10.1007/s41365-017-0207-x
53. T.T. Wang, Y.G. Ma, Nucleon-number scalings of anisotropic flows and nuclear modification factor for light nuclei in the squeeze-out region. Eur. Phys. J. A **55**, 102 (2019). https://doi.org/10.1140/epja/i2019-12788-0. arXiv:2002.06067
54. C.B. Dover, U.W. Heinz, E. Schnedermann et al., Relativistic coalescence model for high-energy nuclear collisions. Phys. Rev. C **44**, 1636–1654 (1991). https://doi.org/10.1103/PhysRevC.44.1636
55. J.L. Nagle, B.S. Kumar, D. Kusnezov et al., Coalescence of deuterons in relativistic heavy ion collisions. Phys. Rev. C **53**, 367–376 (1996). https://doi.org/10.1103/PhysRevC.53.367
56. W. Zhao, K.J. Sun, C.M. Ko et al., Multiplicity scaling of light nuclei production in relativistic heavy-ion collisions. Phys. Lett. B **820**, 136571 (2021). https://doi.org/10.1016/j.physletb.2021.136571
57. Y.H. Feng, C.M. Ko, Y.G. Ma et al., Jet-induced enhancement of deuteron production in pp and p-Pb collisions at the LHC. Phys. Lett. B **859**, 139102 (2024). https://doi.org/10.1016/j.physletb.2024.139102. arXiv:2408.01634
58. X.Y. Zhao, Y.T. Feng, F.L. Shao et al., Production characteristics of light (anti-)nuclei from (anti-)nucleon coalescence in heavy ion collisions at energies employed at the RHIC beam energy scan. Phys. Rev. C **105**, 054908 (2022). https://doi.org/10.1103/PhysRevC.105.054908. arXiv:2201.10354
59. R.Q. Wang, J.P. Lv, Y.H. Li et al., Different coalescence sources of light nucleus production in Au-Au collisions at GeV*. Chin. Phys. C **48**, 053112 (2024). https://doi.org/10.1088/1674-1137/ad2b56. arXiv:2210.10271
60. R.Q. Wang, F.L. Shao, J. Song, Momentum dependence of light nuclei production in p-p, p-Pb, and Pb-Pb collisions at energies available at the CERN large hadron collider. Phys. Rev. C **103**, 064908 (2021). https://doi.org/10.1103/PhysRevC.103.064908
61. R.Q. Wang, Y.H. Li, J. Song et al., Production properties of deuterons, tritons, and ^{3}He via an analytical nucleon coalescence method in Pb-Pb collisions at $\sqrt{s_{\mathrm{NN}}}$ =2.76TeV. Phys. Rev. C **109**, 034907 (2024). https://doi.org/10.1103/PhysRevC.109.034907
62. S. Acharya et al., Light (anti)nuclei production in Pb-Pb collisions at $\sqrt{s_{\mathrm{NN}}}$ =5.02 TeV. Phys. Rev. C **107**, 064904 (2023). https://doi.org/10.1103/PhysRevC.107.064904
63. S. Acharya et al., Measurement of the lifetime and Λ separation energy of $^3_\Lambda$H. Phys. Rev. Lett. **131**, 102302 (2023). https://doi.org/10.1103/PhysRevLett.131.102302. arXiv:2209.07360
64. S. Acharya et al., Measurement of $^3_\Lambda$H production in Pb-Pb collisions at $\sqrt{s_{\mathrm{NN}}}$ =5.02 TeV. Phys. Lett. B **860**, 139066 (2025). https://doi.org/10.1016/j.physletb.2024.139066
65. L.W. Chen, C.M. Ko, B.A. Li, Light cluster production in intermediate-energy heavy ion collisions induced by neutron rich nuclei. Nucl. Phys. A **729**, 809–834 (2003). https://doi.org/10.1016/j.nuclphysa.2003.09.010. arXiv:nucl-th/0306032
66. C.M. Ko, T. Song, F. Li et al., Partonic mean-field effects on matter and antimatter elliptic flows. Nucl. Phys. A **928**, 234–246 (2014). https://doi.org/10.1016/j.nuclphysa.2014.05.016. arXiv:1211.5511
67. L. Zhu, C.M. Ko, X. Yin, Light (anti-)nuclei production and flow in relativistic heavy-ion collisions. Phys. Rev. C **92**, 064911 (2015). https://doi.org/10.1103/PhysRevC.92.064911. arXiv:1510.03568
68. S. Mrowczynski, Production of light nuclei in the thermal and coalescence models. Acta Phys. Polon. B **48**, 707 (2017). https://doi.org/10.5506/APhysPolB.48.707. arXiv:1607.02267
69. A. Kisiel, M. Gałażyn, P. Bożek, Pion, kaon, and proton femtoscopy in Pb-Pb collisions at $\sqrt{s_{\mathrm{NN}}}$=2.76 TeV modeled in (3+1) D hydrodynamics. Phys. Rev. C **90**, 064914 (2014). https://doi.org/10.1103/PhysRevC.90.064914
70. J. Adam et al., Centrality dependence of pion freeze-out radii in Pb-Pb collisions at $\sqrt{s_{\mathrm{NN}}} = 2.76$ TeV. Phys. Rev. C **93**, 024905 (2016). https://doi.org/10.1103/PhysRevC.93.024905
71. H.H. Gutbrod, A. Sandoval, P.J. Johansen et al., Final state interactions in the production of hydrogen and helium isotopes by relativistic heavy ions on uranium. Phys. Rev. Lett. **37**, 667–670 (1976). https://doi.org/10.1103/PhysRevLett.37.667
72. A. Polleri, J.P. Bondorf, I.N. Mishustin, Effects of collective expansion on light cluster spectra in relativistic heavy ion collisions. Phys. Lett. B **419**, 19–24 (1998). https://doi.org/10.1016/S0370-2693(97)01455-X. arXiv:nucl-th/9711011
73. R. Scheibl, U.W. Heinz, Coalescence and flow in ultrarelativistic heavy ion collisions. Phys. Rev. C **59**, 1585–1602 (1999). https://doi.org/10.1103/PhysRevC.59.1585. arXiv:nucl-th/9809092
74. N. Sharma, T. Perez, A. Castro et al., Methods for separation of deuterons produced in the medium and in jets in high energy collisions. Phys. Rev. C **98**, 014914 (2018). https://doi.org/10.1103/PhysRevC.98.014914. arXiv:1803.02313
75. Y.L. Cheng, S. Zhang, Y.G. Ma, Collision centrality and system size dependences of light nuclei production via dynamical coalescence mechanism. Eur. Phys. J. A **57**, 330 (2021). https://doi.org/10.1140/epja/s10050-021-00639-w. arXiv:2112.03520
76. I. Angeli, K.P. Marinova, Table of experimental nuclear ground state charge radii: an update. Atom. Data Nucl. Data Tabl. **99**, 69–95 (2013). https://doi.org/10.1016/j.adt.2011.12.006
77. M. Puccio, CERN-THESIS-2017-338. Ph.D. thesis, Turin U. (2017)
78. P. Chakraborty, A.K. Pandey, S. Dash, Identical-particle (pion and kaon) femtoscopy in Pb-Pb collisions at $\sqrt{s_{\mathrm{NN}}} = 5.02$ TeV with Therminator 2 modeled with (3+1)D viscous hydrodynamics.

Eur. Phys. J. A **57**, 338 (2021). https://doi.org/10.1140/epja/s10050-021-00647-w

79. J. Adams et al., Pion interferometry in Au+Au collisions at $\sqrt{s_{\mathrm{NN}}}$ = 200-GeV. Phys. Rev. C **71**, 044906 (2005). https://doi.org/10.1103/PhysRevC.71.044906. arXiv:nucl-ex/0411036
80. S. Acharya et al., Production of charged pions, kaons, and (anti-) protons in Pb-Pb and inelastic pp collisions at $\sqrt{s_{\mathrm{NN}}} = 5.02$ TeV. Phys. Rev. C **101**, 044907 (2020). https://doi.org/10.1103/PhysRevC.101.044907
81. E. Schnedermann, J. Sollfrank, U.W. Heinz, Thermal phenomenology of hadrons from 200-A/GeV S+S collisions. Phys. Rev. C **48**, 2462–2475 (1993). https://doi.org/10.1103/PhysRevC.48.2462. arXiv:nucl-th/9307020
82. J. Adam et al., Production of light nuclei and anti-nuclei in pp and Pb-Pb collisions at energies available at the CERN large hadron collider. Phys. Rev. C **93**, 024917 (2016). https://doi.org/10.1103/PhysRevC.93.024917. arXiv:1506.08951
83. K.J. Sun, C.M. Ko, B. Dönigus, Suppression of light nuclei production in collisions of small systems at the large hadron collider. Phys. Lett. B **792**, 132–137 (2019). https://doi.org/10.1016/j.physletb.2019.03.033. arXiv:1812.05175
84. P. Kalinak, Strangeness production in Pb-Pb collisions with ALICE at the LHC. PoS EPS-HEP **2017**, 168 (2017). https://doi.org/10.22323/1.314.0168
85. W.B. Chang, R.Q. Wang, J. Song et al., Production of strange and charm hadrons in Pb+Pb collisions at $\sqrt{s_{\mathrm{NN}}} = 502$ TeV †. Symmetry **15**, 400 (2023)
86. C.A. Bertulani, Probing the size and binding energy of the hypertriton in heavy ion collisions. Phys. Lett. B **837**, 137639 (2023). https://doi.org/10.1016/j.physletb.2022.137639. arXiv:2211.12643
87. D.N. Liu, C.M. Ko, Y.G. Ma et al., Softening of the hypertriton transverse momentum spectrum in heavy-ion collisions. Phys. Lett. B **855**, 138855 (2024). https://doi.org/10.1016/j.physletb.2024.138855. arXiv:2404.02701
88. Z. Zhang, C.M. Ko, Hypertriton production in relativistic heavy ion collisions. Phys. Lett. B **780**, 191–195 (2018). https://doi.org/10.1016/j.physletb.2018.03.003
89. H. Clement, On the history of dibaryons and their final observation. Prog. Part. Nucl. Phys. **93**, 195 (2017). https://doi.org/10.1016/j.ppnp.2016.12.004. arXiv:1610.05591
90. J. Pu, K.J. Sun, C.W. Ma et al., Probing the internal structures of pΩ and Ω with their production at the large hadron collider. Phys. Rev. C **110**, 024908 (2024). https://doi.org/10.1103/PhysRevC.110.024908. arXiv:2402.04185
91. T. Iritani et al., $N\Omega$ dibaryon from lattice QCD near the physical point. Phys. Lett. B **792**, 284–289 (2019). https://doi.org/10.1016/j.physletb.2019.03.050. arXiv:1810.03416
92. H. Garcilazo, A. Valcarce, ΩNN and $\Omega\Omega N$ states. Phys. Rev. C **99**, 014001 (2019). https://doi.org/10.1103/PhysRevC.99.014001. arXiv:1901.05678
93. S. Zhang, Y.G. Ma, Ω-dibaryon production with hadron interaction potential from the lattice QCD in relativistic heavy-ion collisions. Phys. Lett. B **811**, 135867 (2020). https://doi.org/10.1016/j.physletb.2020.135867. arXiv:2007.11170
94. L. Zhang, S. Zhang, Y.G. Ma, Production of ΩNN and $\Omega\Omega N$ in ultra-relativistic heavy-ion collisions. Eur. Phys. J. C **82**, 416 (2022). https://doi.org/10.1140/epjc/s10052-022-10336-7. arXiv:2112.02766